Open access • Posted Content • DOI:10.1101/764886

Gradients in the cerebellar cortex enable Fourier-like transformation and improve storing capacity — Source link

Isabelle Straub, Laurens Witter, Laurens Witter, Abdelmoneim Eshra ...+12 more authors

Institutions: Leipzig University, VU University Amsterdam, University of Zurich, University of Strasbourg

Published on: 10 Sep 2019 - bioRxiv (Cold Spring Harbor Laboratory)

Topics: Cerebellar cortex

Gradients in the cerebellar cortex enable Fourier-like transformation and improve storing capacity

Isabelle Straub[1*], Laurens Witter[1,2*], Abdelmoneim Eshra[1*], Miriam Hoidis[1*], Niklas Byczkowicz[1], Sebastian Maaß[1], Igor Delvendahl[1,3], Kevin Dorgans[4], Elise Savier[4], Ingo Bechmann[5], Jens Eilers[1], Martin Krüger[5], Philippe Isope[4], and Stefan Hallermann[1,#]

[1]Carl-Ludwig-Institute for Physiology, Medical Faculty, University of Leipzig, Liebigstrasse 27, 04103 Leipzig, Germany
[2]Department of Integrative Neurophysiology, Center for Neurogenomics and Cognitive Research (CNCR), VU University, De Boelelaan 1085, 1081 HV Amsterdam, The Netherlands
[3]current address: Institute of Molecular Life Sciences, University of Zurich, Winterthurerstrasse 190, 8057 Zurich, Switzerland
[4]Institut des Neurosciences Cellulaires et Intégratives, CNRS, Université de Strasbourg, 8, allée du Général Rouvillois, 67084 Strasbourg, France
[5]Institute of Anatomy, Medical Faculty, University of Leipzig, Leipzig, Germany
* These authors contributed equally to this work
[#] Corresponding author

Abstract

Cerebellar granule cells (GCs) making up majority of all the neurons in the vertebrate brain, but heterogeneities among GCs and potential functional consequences are poorly understood. Here, we identified unexpected gradients in the biophysical properties of GCs. GCs closer to the white matter (inner-zone GCs) had higher firing thresholds and could sustain firing with larger current inputs. Dynamic clamp experiments showed that inner- and outer-zone GCs preferentially respond to high- and low-frequency mossy fiber inputs, respectively, enabling to disperse the mossy fiber input into its frequency components as performed by a Fourier transformation. Furthermore, inner-zone GCs have faster axonal conduction velocity and elicit faster synaptic potentials in Purkinje cells. Neuronal network modeling revealed that these gradients improve spike-timing precision of Purkinje cells and decrease the number of GCs required to learn spike-sequences. Thus, our study uncovers biophysical gradients in the cerebellar cortex enabling a Fourier-like transformation of mossy fiber inputs.

Introduction

Digital audio compression (e.g., 'MP3'; Jayant et al., 1993) and image compression (e.g., 'JPEG'; Wallace, 1992) rely on Fourier transformations, which decompose a signal (e.g., sound amplitude as a function of time or image intensity as a function of space) into its frequency components (power as a function of frequency). By storing these frequency components with different precision depending on psychophysical demands of hearing and seeing, the overall storage capacity can be increased dramatically. In principle, neuronal networks consisting of neurons with varied electrophysiological properties could be suitable for Fourier-like transformations of information. This could benefit processing in neuronal circuits by increasing the signal-to-noise ratio of input signals or by selecting only relevant spectral components of a signal. Interestingly, there are indications that for example pyramidal neurons in visual cortex and in the hippocampus are tuned to different inputs or different input strengths (Cembrowski and Spruston, 2019; Fletcher and Williams, 2019; Soltesz and Losonczy, 2018). However, whether these neuronal networks perform a Fourier-like transform on their inputs remains unknown.

Controlling the timing and precision of movements is considered to be one of the main functions of the cerebellum. In the cerebellum, the firing frequency of Purkinje cells (PCs) (Heiney et al., 2014; Herzfeld et al., 2015; Hewitt et al., 2011; Medina and Lisberger, 2007; Payne et al., 2019; Sarnaik and Raman, 2018; Witter et al., 2013) or the timing of spikes (Brown and Raman, 2018; Sarnaik and Raman, 2018) have been shown to be closely related to movement. Indeed, cerebellar pathology impairs precision in motor learning tasks (Gibo et al., 2013; Martin et al., 1996) and timing of rhythmic learning tasks (Keele and Ivry, 1990). These functions are executed by a remarkably simple neuronal network architecture. Inputs from mossy fibers (MFs) are processed by GCs and transmitted via their parallel fiber (PF) axons to PCs, which provide the sole output from the cerebellar cortex. GCs represent the first stage in cerebellar processing and have been proposed to provide pattern separation and

conversion into a sparser representation of the MF input (recently reviewed by (Cayco-Gajic and Silver, 2019). These MF inputs show a wide variety of signaling frequencies, ranging from slow modulating activity to kilohertz bursts of activity (Arenz et al., 2008; Rancz et al., 2007; Ritzau-Jost et al., 2014; van Kan et al., 1993). Interestingly, in cellular models of the cerebellum, each MF is considered to be either active or inactive with little consideration for this wide range of frequencies (Albus, 1971; Marr, 1969). Furthermore, in these models, GCs are generally considered as a uniform population of neurons.

Here we show that the biophysical properties of GCs differ according to their vertical position in the GC layer. GCs located close to the white matter (inner-zone) selectively transmit high-frequency MF inputs, have shorter action potentials and a higher voltage threshold to fire an action potential compared with GCs close to the PC layer (outer-zone). This gradient of GC properties enables a Fourier-like transformation of the MF input, where inner-zone GCs convey the high-frequency and outer-zone GCs the low-frequency components of the MF input. These different Fourier-like components are sent to PCs by specialized downstream signaling pathways, differing in PF axon diameters, action potential velocity and PC excitatory postsynaptic potential (EPSP) kinetics. Computational simulations show that the biophysical gradients in the GC and molecular layer significantly reduce the number of GCs required to learn a sequence of firing frequencies and accelerate the time required to switch between firing frequencies.

Results

A gradient in the biophysical properties of inner- to outer-zone GCs

To investigate whether GCs are tuned for different frequencies we first investigated the intrinsic membrane properties of GCs from different depths within the GC layer in lobule V of the cerebellum of P21-30 mice. We divided the GC layer into three zones and performed whole-cell current-clamp recordings

from inner- (closest to the white matter), middle- and outer-zone (closest to PCs) GCs (**Figure1A,B**). Upon current injection, inner-zone GCs were less excitable compared with outer-zone GCs (**Figure 1C**). On average, the relationship between the mean number of action potentials and the injected current were surprisingly different for inner- and outer-zone GCs (**Figure 1D**): inner-zone GCs needed higher current injections to fire an action potential (inner: 56.8 ± 2.6 pA vs. middle: 51.2 ± 2.0 pA vs. outer: 39.4 ± 2.0 pA; n = 38, 31, and 38, respectively; $P_{ANOVA} < 0.0001$; **Figure 1E**) and to achieve the maximum firing rate compared with middle- and outer-zone GCs (inner: 224.6 ± 9.8 pA vs. middle: 190.8 ± 9.6 pA vs. outer: 174.3 ± 9.0 pA, respectively; $P_{ANOVA} = 0.0007$; **Figure 1F**). Consistently, inner-zone GCs had a more depolarized threshold for action potential generation compared with middle- and outer-zone GCs (-38.0 ± 0.7 mV vs. -38.2 ± 0.8 mV vs. -41.4 ± 0.6 mV; $P_{ANOVA} = 0.001$; **Figure 1G**) and a lower input resistance (486 ± 27 MΩ vs. 494 ± 27 MΩ vs. 791 ± 63 MΩ; P_{ANOVA} = <0.0001; **Figure 1H**). Furthermore, the capacitance of inner-zone GCs was significantly larger compared to the outer-zone GCs (inner: 5.8 ± 0.2 pF vs. middle: 5.8 ± 0.2 pF vs outer: 4.6 ± 0.1 pF; P_{ANOVA} = <0.0001 **Figure 1I**). In agreement with these findings we observed depolarization block in inner-zone GCs at higher current inputs than for outer-zone GCs (**Figure 1C,D**). Furthermore, a larger delay of the first spike was observed in inner- compared with outer-zone GCs ($P_{T\text{-}Test} = 0.01$; **Figure 1J;** $P_{ANOVA} = 0.0001$; **Figure 1K**). The delay with 60 pA current injection was 48 ± 6 ms for inner-, 38 ± 4 ms for middle-, and 23 ± 2 ms for outer-zone GCs (n = 32, 25, and 37, respectively; note that 6 out of 38 inner-zone GC did not fire an action potential at 60 pA). Finally, the action potential half-width of GCs differed significantly between the three zones (inner: 122 ± 2 µs vs. middle: 137 ± 4 µs vs. outer: 143 ± 4 µs; $P_{ANOVA} = 0.0001$; **Figure 1L**).

To test whether these gradients are specific to lobule V, we investigated GCs in lobule IX. Here, we observed very similar gradients to lobule V (**Figure 1—figure supplement 1**). In short, outer-zone GCs were more excitable and had broader spikes compared with inner-zone GCs. Interestingly, the absolute values

between lobule V and IX differed (**Figure 1—figure supplement 1**), consistent with previously described differences in, e.g., the firing frequency *in vivo* between these two lobules (Witter and De Zeeuw, 2015a; Zhou et al., 2014) and in the differential density of Kv4 and Cav3 channel expression in GCs across different lobules (Heath et al., 2014; Rizwan et al., 2016; Serôdio and Rudy, 1998). Taking the large functional difference between spino- and vestibulo-cerebellum into account (Witter and De Zeeuw, 2015b), these data suggest that different biophysical properties of GCs is likely a conserved mechanism throughout the entire cerebellar cortex, potentially tuning GCs to different frequencies.

Development can have large effects on the physiology of neurons, and GCs in particular undergo profound changes during development (Dhar et al., 2018; Lackey et al., 2018). To exclude confounding effects of developmental stage, we tested whether these gradients were also present at a later developmental stage. Recordings obtained from GCs in lobule V in animals between 80 and 100 days of age showed the very similar gradients as in young animals (**Figure 1—figure supplement 2**). Together, these data show a prominent gradient in the electrophysiological properties of GCs over the depth of the granule cell layer, and that this gradient can consistently be found in different lobules and ages.

Voltage-gated potassium currents are larger at inner-zone GCs

To investigate possible causes for the gradient in the biophysical properties, we investigated voltage-gated potassium (Kv) currents by performing voltage-clamp recordings in outside-out patches from somata of inner- and outer-zone GCs in lobule V (**Figure 2A**). The maximum Kv current was significantly higher in inner-zone GCs (282 ± 29 pA, n = 48) compared with outer-zone GCs (221 ± 28 pA, n = 54, $P_{Mann\text{-}Whitney}$ = 0.02; **Figure 2B**). Neither the steady-state activation curve (**Figure 2C**) nor the degree of inactivation (**Figure 2D**) was different between the two GC populations. Furthermore, steady-state inactivation, which was investigated with different holding potentials, was similar between inner- and outer-zone GCs (**Figure 2—figure supplement 1**). These data suggest that inner- and outer-zone GCs have a similar composition of Kv channels, but inner-

zone GCs have a higher Kv channel density. The here observed larger Kv currents in inner-zone GCs are consistent with the short action potential duration of inner-zone GCs (cf. Figure 1). Thus, our data provide a biophysical explanation for the observed gradient in GC properties.

MF inputs are differentially processed by inner and outer GCs

The gradient within the GC layer creates an optimal range of input strengths for each GC. To test how this gradient impacts the processing of synaptic MF inputs, we performed dynamic clamp experiments to test whether different MF input frequencies differentially affect spiking in inner- and outer-zone GCs (**Figure 3A**). We first recorded excitatory postsynaptic currents (EPSC) from GCs located at inner- or outer-zone of lobule V after single MF stimulation. We found no significant differences in the amplitude nor in the kinetics of EPSCs in inner- and outer-zone GCs (**Figure 3—figure supplement 1**).

Individual MFs span the entire depth of the GC layer, contacting both inner- and outer-zone GCs (Krieger et al., 1985; Palay and Chan-Palay, 1974). Furthermore, GCs are electronically extremely compact neurons and can be considered as a single compartment (D'Angelo et al., 1993; Delvendahl et al., 2015; Silver et al., 1992). Therefore, we could use the dynamic clamp technique to implement the conductance of identical MF signals in inner- and outer-zone GCs based on the measured EPSC kinetics. We first applied input of a single MF with Poisson-distributed firing-frequencies ranging between 30 and 500 Hz for 300 ms duration while changing the resting membrane potential to simulate the large variability of membrane potential of GCs observed *in vivo* (Chadderton et al., 2004). In line with the observed gradients in the electrophysiological properties of GCs, inner-zone GCs fired fewer action potentials compared with outer-zone GCs in response to low-frequency MF inputs at a membrane potential of ~–90 mV (**Figure 3B,C**). In contrast, inner-zone GCs fired more action potentials compared with outer-zone GCs in response to high-frequency MF inputs at a membrane potential of ~–70 mV. *In vivo*, such a depolarization would be caused by less inhibition and/or additional MF inputs. These data suggest that

outer- and inner-zone GCs are specialized for low- and high-frequency MF inputs, respectively.

Fourier-like transformation of MF input frequency

To further test whether inner- and outer-zone GCs can extract different frequency components from a MF input signal, which would resemble a Fourier-transformation, we varied the MF input frequency sinusoidally between 30 and 300 Hz (**Figure 4A**). At a holding potential of -70 mV, inner-zone GCs responded preferentially to high-frequency MF inputs up to 300 Hz, while outer-zone GCs responded preferentially to low-frequency inputs up to 100 Hz. To estimate the optimal frequency at which inner- and outer-zone GCs preferentially fire action potentials, we calculated the phase angle (see Methods). The mean phase angle, at which GC preferentially fired, was 145.9 ± 10.4° for inner-zone (n = 13) and 102.5 ± 18.3° for outer-zone GCs (n = 9) ($P_{T\text{-}TEST}$ = 0.04), representing an average firing frequency of 217 and 100 Hz for inner- and outer-zone GCs, respectively. Thus, the gradient in the biophysical properties enables the cerebellar GC layer to split incoming MF signals into different frequency bands and thereby to perform a Fourier-like transformation of the compound MF input signal.

The position of PFs is correlated with the position of GC somata

A Fourier-like transformation in the GC layer (i.e. a separation of the spectral components of MF signals) could be particularly relevant if downstream pathways are specialized for these spectral components. Early silver-stainings and drawings from Ramón y Cajal indicate that inner-zone GCs give rise to PFs close to the PC layer and outer-zone GCs give rise to PFs close to the pia (Eccles, 1967; Ramón y Cajal, 1911 but see Espinosa and Luo, 2008; Wilms and Häusser, 2015). To test this possibility, we examined the ascending and parallel branches of the GC axon. First, we investigated whether there is a correlation between the relative positions of the PF in the molecular layer and the GC somata in the GC layer. DiI was injected *in vivo* into the GC layer to label GCs and their axons. Several GCs were clearly stained 24h after DiI injection (**Figure**

5A), and the position of their soma and PF in the cerebellar cortex could be measured (**Figure 5B-D**). Even though the length of the ascending GC axon showed considerable variation (196 ± 5.5 µm, range: 144 to 291 µm, n = 39 axons in n = 6 mice), after normalization for the thickness of the molecular and GC layers, GC soma position was significantly correlated with the position of the bifurcation in the GC axon (**Figure 5C,D**; R^2=0.86, P<0.001). These data show that inner- and outer-zone GCs preferentially give rise to inner- and outer-zone PFs, respectively.

Inner-zone PFs have larger diameter and higher action potential propagation velocity

Next, we tested whether PFs, like GCs, have different properties depending on the position within the molecular layer. First, we compared the PF diameters in electron microscopic images of parasagittal sections of mouse cerebellum lobule V and found significantly larger diameters for inner-zone PFs compared to middle- and outer-zone PFs (182 ± 2.6 nm, n = 703 vs. 159 ± 2.0 nm, n = 819 vs. 145 ± 1.7 nm, n = 1085 **Figure 6A-C;** P_{ANOVA}< 0.0001), which is in agreement with previous investigations reported in cat (Eccles et al., 1967), monkey (Fox and Barnard, 1957), and rats (Pichitpornchai et al., 1994).

Axonal diameter is often a strong predictor for axonal conduction speed (Jack et al., 1983). We therefore recorded compound action potentials of PFs in lobule V and compared their conduction speed in the inner-, middle- and outer-zone of the molecular layer (**Figure 6D-F**). We detected a significantly higher velocity in inner-zone PFs compared with in middle- or outer-zone PFs (0.33 ± 0.004 m s^{-1}, n = 8 vs. 0.31 ± 0.005 m s^{-1}, n = 6 vs. 0.28 ± 0.005 m s^{-1}, n = 8; **Figure 6F;** P_{ANOVA} < 0.0001). The absolute velocity and the gradient in the velocity from inner- to outer-zone PFs agree well with previous studies (Baginskas et al., 2009; Vranesic et al., 1994). These results suggest that the inner-zone PFs are specialized for fast signaling, which is consistent with the concept that inner-zone GCs are tuned for high-frequency inputs (cf. Figure 1 and 2).

In addition to the above results obtained from lobule V, similar gradients in both axon diameter and axon conduction speed were found in lobule IX (**Figure 6—figure supplement 1**). This suggests that gradients in axon diameter and axon conduction speed are general features of the cerebellar cortex.

A possible confounder of our results could be an overrepresentation of large-diameter Lugaro cell axons within inner-zone PFs (Dieudonne and Dumoulin, 2000). However, this would predict that the histogram of the axon diameters shows two distinct peaks with varying amplitude. Instead, we observed a single bell-shaped distribution in each PF zone (**Figure 6—figure supplement 2**), arguing that the measured differences between axon diameters were not due to varying contributions from Lugaro cell axons, but reflect the differences between inner-, middle- and outer-zone PFs.

PCs process inner-, middle-, and outer-zone PF inputs differentially

Our data thus far indicate that GCs and PFs are adapted to different MF input frequencies and conduction velocity, respectively. This arrangement could in principle provide PFs with functionally segregated information streams that are differentially processed in PCs. To investigate this possibility, we made whole-cell current-clamp recordings from PCs in sagittal slices of the cerebellar vermis. PCs were held at a hyperpolarized voltage to prevent spiking and to isolate excitatory inputs. Electrical stimulation of the PFs was alternated between inner-, middle- and outer-zones and adjusted to obtain similar amplitude EPSPs in all zones (**Figure 7A,B**). Stimulation of inner-zone PFs resulted in EPSPs (Barbour, 1993; Roth and Häusser, 2001) with shorter rise and decay times compared with EPSPs obtained from stimulating outer-zone PFs ($rise_{20\text{-}80}$: inner: 0.57 ± 0.04 ms, n = 12; middle: 0.93 ± 0.17 ms, n = 4; outer: 1.83 ± 0.33 ms, n = 12 (P_{ANOVA} = 0.009; decay: inner: 21.9 ± 1.5 ms, middle: 39.7 ± 1.1 ms outer: 40.8 ± 4.1 ms; P_{ANOVA} = 0.0004, **Figure 7C**). These results suggest that inner-zone PF inputs undergo less dendritic filtering in PCs compared with outer-zone PF inputs (De Schutter and Bower, 1994a, b; Roth and Häusser, 2001) but see (De Schutter and Bower, 1994c). To investigate high-frequency inputs to PCs, we elicited five

EPSPs at 100 Hz and 500 Hz (**Figure 7D,E**). Individual EPSPs evoked from inner-zone PFs showed clear individual rising phases and peaks between each stimulus and less summation compared with outer-zone PFs (**Figure 7D-F**). These results suggest that inner-zone PFs can transmit timing information more faithfully compared with outer-zone PFs and thus control spike timing of PCs more precisely.

The observed neuronal gradients increase storing capacity and improve temporal precision of PC spiking

Thus far we have described a prominent gradient in the electrophysiological properties of GCs over the depth of the GC layer that enables inner- and outer-zone GCs to preferentially respond to high- and low-frequency inputs, respectively. The different frequency components are transferred via specialized PFs, which enable PCs to interpret high-frequency signals rapidly at the base of their dendritic trees and low-frequency signals slowly at more distal parts of their dendritic trees (**Figure 8A**).

To address the functional implications of these gradients in the GC and molecular layer, we performed computational modeling of a neuronal network of the cerebellar cortex with integrate-and-fire neurons. The model consisted of one PC and varying number of GCs and MFs (**Figure 8A**). GCs received randomly determined MF inputs with either tonic (Arenz et al., 2008; van Kan et al., 1993) or bursting (Rancz et al., 2007) *in vivo*-like spiking sequences. By changing the synaptic weights of the GC to PC synapses, the PC had to acquire a target spiking sequence with regular 80-, 40- and 120-Hz firing (**Figure 8B**). The algorithm for changing the synaptic weights was a combination of a learning algorithm based on climbing-fiber-like punishments and an unbiased minimization algorithm (see Methods).

We first compared a model without gradients, where the parameters were set at the average of the experimentally determined values, with a model including all experimentally determined gradients (black and red, respectively, throughout

Figure 8). To measure the difference between the final PC spiking and the target sequence we calculated van Rossum errors using a time constant of 30 ms (Rossum, 2001) **Figure 8C-E**). With increasing number of GCs, the final PC spiking sequence resembled the target sequences increasingly better, as illustrated by an average spiking histogram from many repetitions with different random sets of MF inputs for models consisting of 100 and 1000 GCs (**Figure 8B**). As expected, the average minimal van Rossum error (for many repetitions with different random sets of MF inputs) decreased with increasing number of GCs (**Figure 8C**). For all sizes of the GC population, the average minimal van Rossum error was significantly smaller in the model containing all the experimentally determined gradients compared with the model without any gradients. For example, to obtain the spiking precision of the model containing 400 GCs with all gradients, the model without gradients required 800 GCs (cf. red arrows in **Figure 8C**). This indicates that for a cerebellum exploiting gradients in the GC layer, the number of GCs can at least be halved to obtain a certain temporal precision compared with a cerebellum containing no gradients.

To investigate the relative contribution of each of the gradients, we tested models containing each gradient in isolation, resulting in intermediate van Rossum errors (blue, yellow, and green in **Figure 8C,D**). The average relative differences between the models across all sizes of the GC populations suggest an almost additive behavior of the individual gradients to the overall performance (**Figure 8E**).

To further investigate the interplay of the different gradients, we investigated a model containing all gradients, but the connectivity between GCs, PF action potential speed, and PC EPSP kinetics were randomly intermixed (red dashed lines in Figure 8C-E). The network benefits from these intermixed gradients, but maximum optimization can only be obtained with correct connectivity (**Figure 8E**).

The time constant of the van Rossum error can be decreased or increased to investigate spike timing or slower changes in firing rate, respectively. The impact of the gradients increased with increasing time constant (**Figure 8—figure supplement 1A,B**), indicating that rate coded signaling especially benefits from the here described gradients. To specifically test the effect of gradients on the cerebellum's ability to switch between firing frequencies, we made sigmoid fits around the times of firing rate changes. The transition time (t_T; see methods) from these fits showed that models with all gradients showed on average 20% faster switching between firing frequencies than models without any gradients (**Figure 8—figure supplement 1C-F**).

To further test the influence of gradients on efficient cerebellar processing, we repeated the modeling experiments but used a target sequence with a firing pause (i.e. 80, 0, and 120 Hz instead of 80, 40, and 120 Hz) resulting in similar van Rossum errors and transition time **(Figure 8—figure supplement 1G-M**). A pause in firing enabled us to quantify the temporal error at the start and the end of the pause (**Figure 8—figure supplement 1N-Q**), because these spike times have been proposed to be of particular relevance for behavior (Hong et al., 2016). Both measures (transition time and temporal error in pause beginning and end) revealed similar results compared with the van Rossum measure, indicating that the speed of 'frequency-switching' and the temporal spiking precision of PCs critically depend on the here described gradients. Thus, our modeling results show that experimentally determined gradients improve the spiking precision, accelerate 'frequency-switching', and increase the storing capacity of the cerebellar cortex.

Discussion

In this study, we describe a gradient in the biophysical properties of superficial to deep GCs, which enables the GC layer to perform a Fourier-like transformation of the MF input. Furthermore, we show that the downstream pathways from GCs

to PCs are specialized for transmitting the frequency band for which the corresponding GCs are tuned to. Finally, computational modeling demonstrates that both the gradients in the GC layer and the specialized downstream pathways improve the spiking precision, accelerate the change of firing frequency of PCs, and increase storing capacity in the cerebellar cortex.

Fourier-like transformation in the cerebellar cortex

Our data demonstrate that outer-zone GCs preferentially fire during MF input with low frequency ('low-frequency' GCs, magenta in **Figure 9A**), whereas inner-zone GCs preferentially fire during MF input with high frequency ('high-frequency' GCs, green in **Figure 9A**). The separation of a signal into its frequency components resembles a Fourier transformation (**Figure 9B**). The analogy with a Fourier transformation has the limitations that (1) a single MF cannot transmit two frequencies simultaneously but only separated in time (cf. example in **Figure 9A**) and (2) concurrent inputs from two MFs with different frequencies synapsing onto a single GC cannot be separated. Yet, our data indicate that the entire GC layer with several MFs sending various frequencies to numerous GCs can execute a Fourier-like transformation. In analogy to the dispersion of white light in an optical prism into its spectral components, the broadband MF signal is separated into its spectral components with inner- to outer-zone GCs preferentially transmitting the high- to low frequency components, respectively. Such a separation offers the chance to process each frequency component differentially. Indeed, in the molecular layer, the high-frequency components of the MF signal are sent via rapidly conducting axons to proximal parts of the PC dendritic tree. This allows fast (phasic) signals to have a strong and rapid impact on PC firing. On the other hand, low-frequency components of the MF signal are conducted more slowly and elicit slower EPSPs, allowing slow (tonic) signals to have a modulatory impact on PC firing. Our data indicate that, in analogy to the increased storing capacity of digital audio and image compression (Jayant et al., 1993; Wallace, 1992), the combination of a Fourier-like transformation in the GC layer and specialized downstream signaling pathways in the molecular layer dramatically reduces the number of required GCs for precise PC spiking (**cf. Figure 8**).

Furthermore, our data support the 'adaptive filter' theory of the cerebellum, where broadband MF input is differentially filtered by GCs (Dean et al., 2010; Fujita, 1982; Singla et al., 2017). Within this framework, our data indicate a gradient in the band-pass filtering properties of GCs. Furthermore, our data could provide an additional explanation for improved motor learning by elevated background activity of MFs (Albergaria et al., 2018), because the elevated MF activity will help overcoming the high threshold of inner-zone GCs, which rapidly and effectively impact PCs via fast conducting PFs at the proximal dendrite.

Axes of frequency specialization in the cerebellum

There are at least two axes of heterogeneity in the cerebellar cortex. First, Zebrin stripes can be observed as parasagittal zones ('medio-lateral' axis) in cerebellar cortex (Apps et al., 2018). Firing rate, firing regularity, synaptic connectivity and even synaptic plasticity seems to differ between PCs in zebrin positive and negative zones (Valera et al., 2016; Wadiche and Jahr, 2005; Xiao et al., 2014; Zhou et al., 2014). Second, there is a lobular organization ('rostro-caudal' axis) as shown here by the functional differences between lobules V and IX (**Figure 1—figure supplement 1**). GCs in lobule IX are tuned to lower frequencies than GCs in lobule V. These findings are largely in line with previous investigations (Heath et al., 2014; Witter and De Zeeuw, 2015a; Zhou et al., 2014), where the anterior cerebellum was identified to process high-frequency or bursting signals, while the vestibulo-cerebellum mainly processed lower frequency or slowly-modulating inputs. Furthermore, the optimal time intervals for introduction of spike timing dependent plasticity differ between the vermis and the flocculus (Suvrathan et al., 2016).

In addition to these two known axes of heterogeneity, we described an axis that is orthogonal to the surface of the cerebellar cortex. This 'depth' axis causes inner-zone GCs to be tuned to higher frequencies than outer-zone GCs. This frequency gradient along the 'depth'-axes is in line with recently described connections of MFs and PC, which specifically target GCs close to the PC layer (Gao et al., 2016; Guo et al., 2016). These connections send slow feedback

signals to the outer-zone GCs, which — according to our framework — are ideally suited to process such slow modulatory signals. Independent of these specialized feedback pathways, MFs exhibit heterogeneity (Chabrol et al., 2015; Bengtsson and Jörntell, 2009). Our data indicate that each type of the heterogeneous MF inputs is split into its frequency components along the depth axis. Our results furthermore predict that superficial GCs, such as the ones imaged recently in the investigation of eye-blink conditioning and reward representation in the cerebellar cortex (Giovannucci et al., 2017; Wagner et al., 2017), would preferentially convey low-frequency signals to PCs and might not be representative for the full range of frequencies present over the depth of the GC layer.

Thus, including this new 'depth' axis, there are three orthogonal axes along which the cerebellar cortex is tuned for preferred frequency, indicating the importance of proper frequency tuning of the circuitry.

The role of inhibition

In the current study we did not investigate molecular layer interneurons, which can have large impact on PC spiking (Blot et al., 2016; Dizon and Khodakhah, 2011; Gaffield and Christie, 2017; Mittmann et al., 2005; Sudhakar et al., 2017). However, the spatial arrangement of stellate and basket cell interneurons is consistent with our framework. Although the dendrites of molecular layer interneurons can span the entire molecular layer, the dendrites of basket cells seem to be preferentially located at the inner-zone of the molecular layer (Palkovits et al., 1971; Rakic, 1972), which positions them ideally to receive rapid high-frequency signals of inner-zone PFs. Consistently, they impact PC firing rapidly and efficiently via their pinceaus (Blot and Barbour, 2014). Furthermore, the dendrites of a subset of stellate cells (with their somata located in the outer-zone molecular layer) are preferentially located at the outer-zone molecular layer (Palkovits et al., 1971; Rakic, 1972), which positions them ideally to receive modulatory low-frequency signals and elicit slow IPSPs in PCs. Furthermore, molecular layer interneurons seem to represent a continuum along the vertical

axis, with a correlation between the vertical location of the soma, axonal boutons, and dendrite location (Sultan and Bower, 1998), which is consistent with the here-described continuum of biophysical properties along the vertical axis of the cortex. Incorporating molecular layer interneurons, their synaptic plasticity and their potential gradients into the frequency-dispersion framework may show a further increase in the dynamic range of frequency separation within the cerebellar cortex over what we have described here (Gao et al., 2012).

Functional implications for the cerebellum

In general, our anatomical and electrophysiological data, combined with our modeling results, show that inner-zone GCs convey high-frequency signals from MFs via rapid pathways to PCs with little filtering. This is in contrast to outer-zone GCs that are tuned to lower frequencies, and which signals undergo more filtering in the PC. These results suggest that the sparse code of GCs (Albus, 1971; Billings et al., 2014; Marr, 1969) is in part caused by different frequency tuning of GCs.

MF firing frequencies range from <1 to ~1000 Hz (Arenz et al., 2008; Chadderton et al., 2004; Jörntell and Ekerot, 2006; Rancz et al., 2007; van Kan et al., 1993). Many previous modeling studies investigating cerebellar function considered the activity of each MF as a constant digital value (Albus, 1971; Babadi and Sompolinsky, 2014; Brunel et al., 2004; Clopath et al., 2012; Marr, 1969), a constant analog value (Chabrol et al., 2015; Clopath and Brunel, 2013), or spike sequences with constant frequency (Billings et al., 2014; Cayco-Gajic et al., 2017; Steuber et al., 2007). We focused on the time-varying aspects of MF integration in GCs, and therefore implemented a model with a corresponding large range of MF input frequencies that could change over time. It would be interesting to elucidate in, as much previous models, consisting of more uniform MF inputs, would benefit from the here-observed biophysical gradients.

To implement these gradients in a model we used a simplified cerebellar circuitry that does not consider active dendrites (Llinás and Sugimori, 1980) or the tonic

activity of PCs (Raman and Bean, 1997). It will therefore be interesting to investigate if the here-observed gradients in the GC and molecular layer improve the performance of more complex models of the cerebellar cortex (De Schutter and Bower, 1994a; Garrido et al., 2013; Masoli et al., 2015; Medina et al., 2000; Rossert et al., 2015; Spanne and Jörntell, 2013; Steuber et al., 2007; Sudhakar et al., 2017; Walter and Khodakhah, 2009; Yamazaki and Tanaka, 2007). Furthermore, it remains to be investigated whether gradients in the GC layer also improve models that aim to explain tasks such as eye-blink conditioning (Mauk and Buonomano, 2004) and vestibulo-ocular reflexes (du Lac et al., 1995)

Our model simulated the learning that PCs undergo to acquire specific firing frequencies in response to GC input. PC firing rate and spiking precision have been shown to be closely related to movement (Brown and Raman, 2018; Sarnaik and Raman, 2018). Our results show that the same temporal spiking precision or the same frequency switching speed can be obtained with approximately half the number of GCs when GC gradients are implemented (**Figure 8**). Taking into account the large number of cerebellar GCs in the brain (Herculano-Houzel, 2009; Williams and Herrup, 1988), a significant reduction in the number of GCs could represent an evolutionary advantage to minimize neuronal maintenance energy (Howarth et al., 2012; Isler and van Schaik, 2006). Therefore, the dramatic increase in storing capacity for precise PC spiking provides an evolutionary explanation for the emergence of gradients in the neuronal properties.

Functional implications for other neural networks

Based on the described advantages of the Fourier transformation for rapid and storing-efficient information processing, we hypothesize that other neural networks also perform Fourier-like transformations and use segregated frequency-specific signaling pathways. To our knowledge this has rarely been shown explicitly, but similar mechanisms might operate, for example, in the spinal cord network: descending motor commands from the pyramidal tract send broadband signals to motoneurons with different input resistances resulting from

differences in size. This enables small motoneurons to fire during low-frequency inputs and large motoneurons only during high-frequency inputs (Henneman et al., 1965). Furthermore, specialized efferent down-stream signaling pathways innervate specific types of muscles with specialized short-term plasticity of the corresponding neuromuscular junctions (Wang and Brehm, 2017).

In the hippocampus, frequency preferences of hippocampal neurons are well established enabling segregation of compound oscillatory input into distinct frequency components (Pike et al., 2000). Furthermore, there is increasing evidence that previously considered homogeneous population of neurons exhibit gradients in the neuronal properties (Cembrowski and Spruston, 2019), such as the intrinsic electrical properties and synaptic connectivity in CA3 pyramidal neurons (Galliano et al., 2013). The heterogeneity furthermore enables functional segregation of information streams for example in CA1 pyramidal neurons (Soltesz and Losonczy, 2018). Finally, in the neocortex, gradients in anatomical and biophysical properties were recently uncovered (Fletcher and Williams, 2019).

In summary, our findings contribute to the growing body of evidence that the neurons of a cell layer can exhibit systematic functional heterogeneities with differential tuning of neurons along gradients. Our data furthermore suggest that such gradients facilitate complex transformation of information, such as Fourier-like transformations, to cope with a broad temporal diversity of signals in the central nervous system.

Material and Methods

Electrophysiology

Parasagittal 300-µm thick cerebellar slices were prepared from P21–P30 (young animals) or from P80-P100 (old animals) C57BL/6 mice of either sex as described previously (Ritzau-Jost et al., 2014);(Delvendahl et al., 2015). Animals were treated in accordance with the German and French Protection of Animals

Act and with the guidelines for the welfare of experimental animals issued by the European Communities Council Directive. The extracellular solution for the whole-cell measurements contained (in mM): NaCl 125, $NaHCO_3$ 25, glucose 20, KCl 2.5, $CaCl_2$ 2, NaH_2PO_4 1.25, $MgCl_2$ 1 (310 mOsm, pH 7.3 when bubbled with Carbogen (95%O_2/5%CO_2)). For outside-out measurements of potassium currents (Figure 2), 150 µM $CdCl_2$ and 1 µM TTX were added to the external solution to block voltage-gated calcium channels and sodium channels, respectively. The intracellular solution contained in mM: K-Gluconate 150, NaCl 10, K-Hepes 10, Mg-ATP 3, Na-GTP 0.3, EGTA 0.05 (305 mOsm, pH 7.3). A liquid junction potential of +13 mV was corrected for. All electrophysiological measurements were performed with a HEKA EPC10 amplifier (HEKA Elektronik, Lambrecht/Pfalz, Germany) under control of the Patchmaster software. All measurements were performed at 34–37°C.

Current clamp recordings in GCs

Action potentials were evoked in current-clamp mode by current pulses (amplitude 20–400 pA, duration 300 ms). To determine the input resistance, subthreshold current pulses were applied from -20 to + 20 pA in 2 pA steps. The resistance of the solution-filled patch-pipettes was between 6–12 MΩ and the mean series resistance was not compensated during the measurement. Data were sampled at 200 kHz.

Outside-out recordings in GCs

To reliably clamp potassium currents from the soma of GCs (**Figure 2**), potassium currents were measured in outside-out patches pulled from the soma of inner and outer GCs by applying 10 ms voltage steps from −90 to +60 mV with 10 mV increments at an intersweep interval of 1 s. The intersweep holding potential was −90 mV. Data were sampled at 100 kHz.

Compound action potentials in PFs

For the detection of compound action potentials in PFs, two pipettes (tip

resistances 1–4 MΩ) filled with extracellular solution and connected to the patch-clamp amplifier were positioned within the molecular layer of horizontally cut slices of the cerebellar vermis. The average distance between two recording electrodes was 143 ± 5 µm. Compound action potentials were evoked by voltage stimulation (100 V) for 100 µs with a third pipette connected to an accumulator powered stimulation device (ISO-Pulser ISOP1, AD-Elektronik, Buchenbach, Germany). 40 to 80 stimulations delivered at 1 Hz were averaged and analyzed.

Excitatory postsynaptic potentials in PC

Excitatory postsynaptic potentials (EPSPs) in PC were elicited by voltage stimulation of the PFs within the inner, middle or outer third of the molecular layer from horizontally cut cerebellar slices (Figure 7). 10 µM SR95531 was added to the external solution to block $GABA_A$ receptors. The stimulation pipette was filled with extracellular solution, and the voltage was adjusted between 6 to 25 V to elicit EPSPs with an amplitude between 1 and 2 mV. EPSPs were measured after a single 100 µs voltage stimulation or 5 stimulations (100 µs duration) at a frequency of 100 and 500 Hz. Averages of 30 trains per stimulation protocol were used for data analysis.

Excitatory postsynaptic currents in GCs

To measure evoked EPSCs from GCs (**Figure 3—figure supplement 1**), 90-100 days-old mice were used. GCs from inner- or outer-zone from lobule V were held at resting conditions and MF axons were stimulated at 1 Hz with a second pipette. The average stimulation voltage was 36 ± 3 V for outer-zone GCs and 37 ± 3 V for inner-zone GCs.

Dynamic Clamp of MF conductance in GCs

In order to analyze the response of GCs on *in-vivo* like MF inputs, we used a dynamic clamp implemented with the microcontroller Teensy 3.6 (https://www.pjrc.com) as described by Desai et al. (Desai et al., 2017). The Teensy was programmed using the Arduino integrated development environment

with the code provided by Desai et al (2017) and modified for our need as described in the following.

The time course of MF conductance was

$$G_{EPSC}(t) = G_{max}\, A_{norm} \left(-e^{-\frac{t}{\tau_r}} + \sum_{i=1}^{3} a_i e^{-\frac{t}{\tau_i}} \right)$$

where the exponential rise time (τ_r) was 0.1 ms, the decay time constants (τ_1, τ_2, and τ_3) were 0.3, 8, and 40 ms, respectively, and the relative amplitude of the decay components (a_1, a_2, and a_3) were 0.7, 0.26, and 0.04, respectively. The peak conductance (G_{max}) was 1 nS (Hallermann et al., 2010) and the normalization factor (A_{norm}) was 0.518, which was numerically calculated to obtain a peak amplitude of 1. The kinetics of the MF conductance were chosen to reproduce the measured mixed AMPA and NMDA EPSC kinetics of single EPSCs (**Figure 3—figure supplement 1**) and trains of EPSCs (Baade et al., 2016). The short-term plasticity during Poisson sequence of spikes was implemented by changing G_{max} according to a simple phenomenological model (Tsodyks and Markram, 1997) assuming a release probability p_{r0} of 0.4 (Ritzau-Jost et al., 2014). Facilitation was implemented as an increase in the release probability according to $p_r = p_r + 0.2*(1- p_r)$ and decaying back to p_{r0} with a time constant of 12 ms (Saviane and Silver, 2006). Depression was implemented according to a recovery process with a time constant of 25 ms, which approximates a biexponential recovery process of 12 ms and 2 s (Hallermann et al., 2010; Saviane and Silver, 2006). The resulting short-term plasticity reproduced previously obtained data with regular spiking ranging from 20 to 1000 Hz (Baade et al., 2016; Hallermann et al., 2010; Ritzau-Jost et al., 2014).

The microcontroller was programmed to implement the MF conductance and its short-term plasticity with Poisson distributed spike times with a constant frequency ranging from 30 to 500 Hz for 300 ms (Figure 3). In each cell, each frequency was applied five times.

To investigate the response to sinusoidally varying input frequencies (Figure 4), the target frequency of the Poisson process (F) was varied on a logarithmic scale according to:

$$F(t) = exp\left(\log(F_{min}) + \left(\log(F_{max}) - \log(F_{min})\right)\left(0.5 + 0.5sin(2\pi t/T)\right)\right)$$

where the minimal and maximal frequency (F_{min} and F_{max}) were 30 and 300 Hz, respectively, and the duration of the sine wave cycle (T) was 1 s. In each cell, 10 cycles were applied consecutively. The histogram of the spike times (Figure 4B) was averaged across the last six cycles of all cells. The vector strength and phase angle (Kan et al., 1993) were calculated as the absolute value and the argument of the complex number ρ ($i = \sqrt{-1}$):

$$\rho = \frac{1}{N}\sum_{n=1}^{N} e^{i2\pi\frac{t_n}{T}}$$

where t_n are the spike times of all N spikes per experiment and T the cycle duration (1 s).

Electron Microscopy

Four C57BL/6 mice of either sex with an age between P23–P28 were sacrificed, followed by transcardial perfusion with saline and consecutively a fixative containing 4% paraformaldehyde and 2% glutaraldehyde in phosphate-buffered saline (PBS). After removal of the brain, the tissue was allowed to post-fix over night at 4°C and sagittal sections of the cerebellum were prepared at a thickness of 60 µm using a Leica microtome (Leica Microsystems, Wetzlar, Germany). The sections were stained in 0.5% osmium tetroxide in PBS for 30 min followed by dehydration in graded alcohol and another staining step with 1% uranyl acetate in 70% ethanol. After further dehydration, the tissue was embedded in durcupan (Sigma-Aldrich), which was allowed to polymerize for 48 h at 56°C between coated microscope slides and cover glasses. Regions of interest were identified by light microscopy, cut and transferred onto blocks of durcupan to obtain ultra-

thin sections using an Ultramicrotome (Leica Microsystems). Ultra-thin sections were transferred onto formvar-coated copper grids and stained with lead citrate. Ultrastructural analysis was performed using a Zeiss SIGMA electron microscope (Zeiss NTS, Oberkochen, Germany) equipped with a STEM detector and ATLAS software.

Measurement of parallel-fiber axon diameter

Electron micrographs were manually analyzed in a blind manner (numbered by masked randomization) and each micrograph was divided into eight identically sized fields. The diameter of each parallel-fiber axon was measured as the longest chord in one or two of these fields. Cross sections with visible active zones or mitochondria were excluded from analysis.

DiI Injections and GC tracking

Six P20 CD1 mice were anesthetized with isoflurane (4%). An incision of the skin to expose the skull and a hole was manually drilled using a 25G needle above the desired injection site. Injections of small amounts of DiI (1,1-dioctadecyl-3,3,3,3 tetramethylindocarbocyanine perchlorate, ThermoFisher Scientific, 10% in N,N-dimethylformamide) were performed using a broken glass pipette connected to a picospritzer II (Parker Instrumentation). 24 h after injection, animals were sacrificed and transcardially perfused with 4% paraformaldehyde in PBS. The cerebellum was dissected, fixed overnight, and embedded in 4% agarose in PBS. 150-µm thick sections were then cut in the transverse or sagittal plane using a vibratome (VT1000, Leica microsystems). Z-Stacks (1 µm steps) were acquired using a confocal microscope (Leica SP5 II, 63x objective). GCs were traced from their soma to the axonal bifurcation of PFs. (Average stack depth: 84 ± 20 µm). GC axons were reconstructed using the 'Simple Neurite Tracer' plugin (Longair et al., 2011) in Fiji (ImageJ, NIH, USA). This plugin allowed us to assess the continuity of axons between several cross-sections. GC ascending axons were then fully traced and measured within the Z-limits of image sections. The size of the different layers of cerebellar cortex was

reconstructed in each Z-stack. To avoid variability, all distances were normalized to the corresponding molecular layer height.

Data analysis

Data were analyzed using custom-written procedures in Igor Pro software (WaveMetrics, Oregon, USA). Intrinsic properties of GCs were determined from the injected currents that elicited the largest number of action potentials. The action potential threshold was defined as the membrane voltage at which the first derivative exceeded 100 V s^{-1}, the minimal action potential peak was set as -20 mV and the minimal amplitude to 20 mV. All action potentials with a half-width smaller than 50 µs and larger than 500 µs were excluded. Action potential frequency and half-width were calculated from the first three action potentials. Membrane capacitance, resting membrane potential and series resistance were read from the amplifier software (HEKA) after achieving the whole-cell configuration. Input resistance (R_{in}) was analyzed from alternating subthreshold current injections from -20 to 20 pA (2 pA steps). The voltage was plotted against injected current and a spline interpolation was performed to obtain the slope at the holding membrane potential (0 pA current injection).

Peak-current from outside-out patches was determined from voltage steps (−90 to +60 mV) with Fitmaster software (HEKA). Steady-state inactivation was determined from the last 2 ms of the respective sweep. Cells were only included if 50 pA < I_{max} < 1 nA to exclude potential whole-cell measurements and membrane-vesicles.

EPSP measurements from PCs and EPSC measurements from GCs were analyzed with the Fitmaster software (HEKA). For PC EPSPs, 20-80% rise time and time to peak were determined from the average of 30 individual single EPSPs. GCs EPSCs were averaged from 25 traces. To obtain the decay kinetics, single EPSPs/EPSCs were fitted with either one or two exponentials. The weighted time constant was calculated as:

719 $$\tau_w = \frac{A_{slow}\,\tau_{slow} + A_{fast}\,\tau_{fast}}{A_{slow} + A_{fast}}$$

720 Paired-pulse ratio was determined between the first and the 5th EPSP after
721 stimulation with 100 Hz trains. Single EPSCs from inner- and outer-zone GCs
722 were averaged and fitted with two exponentials. The decay kinetics and
723 amplitude of the grand-average was used to implement the MF EPSCs for the
724 Dynamic Clamp.
725
726 **Neuronal networking modeling**
727 The neuronal network consisted of varying numbers of MF inputs, GCs and one
728 PC and was implemented in Matlab (The MathWorks, Inc, Natick,
729 Massachusetts, R2017a). For each simulation, a random set of MF inputs was
730 generated. This input was then fed to a layer of integrate-and-fire GCs. A
731 modeled PC then used the output of these GCs for trial-to-trial learning. The PF-
732 to-PC synaptic weights were optimized with the aim to make the PC spiking
733 sequence similar to the target sequence. In the following, each component of the
734 model is explained in detail.
735
736 *MF inputs*
737 To simulate *in vivo* like MF firing patterns, half of the MFs fired tonically (van Kan
738 et al., 1993) and the other half fired bursts (Rancz et al., 2007). All MF spike
739 trains were modeled first by generating a 'threshold trace'. For tonically firing
740 MFs, this threshold trace was a Gaussian function with a peak and standard
741 deviation chosen from uniform distributions ranging between 10 and 100 Hz and
742 0.2 and 0.5 s respectively, and a peak time point between 0 and 0.5 s. For burst
743 firing MFs, the threshold trace was an exponential function with a peak randomly
744 chosen between 600 and 1200 Hz, a decay time constant of 30 ms and a peak
745 between 0 and 0.5 s. The threshold trace was then evaluated against random
746 numbers from a uniform distribution to determine the occurrence of a spike. To
747 accelerate the simulations the sampling time interval was 1 ms.
748

GC properties

GCs were implemented as integrate and fire models with the following parameters: the membrane resistance was linearly varied between 450 MΩ for inner GCs to 800 MΩ for outer GCs (Figure 1H) and the threshold was linearly varied between -37 mV for inner GCs to -42 mV for outer GCs (Figure 1G). For the models without the GC gradient, these values were set to the mean of the values for the inner and outer GC (i.e. 625 MΩ and -39 mV). The reset potential was set to -90 mV and the membrane potential to -80 mV.

PF properties

To simulate a different action potential propagation speed, the GC spike times were delayed by a value linearly varied between 0 for inner and 3 ms for outer GCs. The delay was calculated as the difference in conduction time required to travel 5 mm with a speed of 0.28 and 0.33 m s^{-1} (Figure 4F). Even with this anatomically rather too large PF length (Harvey and Napper, 1991), the PF propagation speed has only a small impact on the model performance (see e.g. blue lines and bars in Figure 7C-E), arguing against a big impact of PF conduction delays (Braitenberg et al., 1997) at least in our model approach.

Synaptic connections and properties

Each MF was connected to 10 GCs and each GC received 2 MF inputs, i.e. the number of MF was 1/5 of the number of GCs. Since our model consists only of 'active' MFs, we chose only 2 and not 4 MFs per GCs (Billings et al., 2014). The MF to GC synapse was implemented as a model with one pool of vesicles with a release probability of 0.5 and a vesicle recruitment time constant of 13 ms (Hallermann et al., 2010). Synaptic facilitation was implemented by increasing the release probability after each spike by 0.2 decaying to the resting release probability with a time constant of 12 ms (Saviane and Silver, 2006). The synaptic conductance had exponential rise and decay time constants of 0.1 and 2 ms, respectively, and a peak amplitude of 1.9 nS (Silver et al., 1992). Correspondingly, the GC to PC synapse was implemented as a model with one

pool of vesicles with a release probability (p_{r0}) of 0.4 and a vesicle recruitment time constant of 50 ms. Synaptic facilitation was implemented by increasing the release probability after each spike by 0.2 decaying to the resting release probability with a time constant of 50 ms (Doussau et al., 2017; Isope and Barbour, 2002; Valera et al., 2012). The synaptic conductance had exponential rise time constant between 0.5 and 2 ms and decay time constant between 17.5 and 70 ms for inner- and outer-zone GCs, respectively (Figure 6). The peak amplitude was adjusted to equalize the charge of the EPSC and to generate an approximately correct number of PC spikes (with the initial start values, i.e. all GC to PC synaptic weight factors = 1) by linearly varying between 0.5 and 0.15 nS for inner- and outer-zone GCs, respectively.

PC properties

The PC was implemented as an integrate and fire model with a membrane resistance of 15 MΩ, resting membrane potential of -50 mV, and a firing threshold of -45 mV. Spontaneous firing of PCs (Raman and Bean, 1997) was not implemented, and the only inputs to drive PCs to threshold were the GC-to-PC EPSCs.

Target sequence and van Rossum measure

Based on *in vivo* firing patterns (Witter and De Zeeuw, 2015a), an arbitrary target firing sequence of 80, 40, and 120 Hz for 300, 100, and 100 ms, respectively, was chosen. The distance between the PC and the target spiking sequence was quantified with the van Rossum error (van Rossum, 2001). Both spiking sequences were convolved with an exponential kernel with a decay time constant of 30 ms (or values ranging from 2 to 300 ms in (**Figure 8—figure supplement 1A,B**). The van Rossum error was defined as the integral of the square of the difference between these two convolved traces. We also tested another algorithm to calculate the van Rossum error (Houghton and Kreuz, 2012), which C++ code was taken from http://pymuvr.readthedocs.io/ and incorporated into Matlab via the MEX function and results were comparable.

Learning and minimization algorithm

For each random set of MF inputs, the GC to PC synaptic weights were changed according to the following algorithm with the aim to minimize the van Rossum error between the PC spiking sequence and the target sequence. The initial values of the synaptic weights were 1, and values were allowed to change between 0 and 100. First, an algorithm was used that was based on supervised learning (Raymond and Medina, 2018) to punish the GCs that have spikes that precede unwanted PC spikes. Subsequently, an unbiased optimization of the GC to PC synaptic weight was performed using the patternsearch() algorithm of Matlab to minimize the van Rossum error. To increase the chance that a global (and not local) minimum was found, the minimization of the routine was repeated several times with random starting values. Other optimization routines such as a simplex [(fminsearch() of Matlab) or a genetic algorithm (ga() of Matlab)] revealed similar results. To exclude the possibility that the differences in the minimal van Rossum error between models with and without gradients were due to a bias in our learning algorithm, we performed a set of simulations with networks consisting of less than 100 GCs, in which we skipped the learning algorithm and only used unbiased minimization algorithm. This resulted in similar difference in the minimal van Rossum error between models with and without gradients, indicating that the learning algorithm was not biased towards one type of model. For networks with consisting of more than 100 GCs the pre-learning was required to facilitate the finding of the global minimum.

Analysis of modeling results

300 different sets of random MF inputs were used to determine 300 statistically independent minimal van Rossum values for each of the models with different number of GCs and different number of implemented gradients (illustrated as mean ± SEM in Figure 7C). Comparing different models with the same set of MF input (using the nonparametric paired Wilcoxon signed-rank statistical test) the difference was significant ($p<0.001$) for all of the models and all number of GCs.

The van Rossum errors were then normalized to the mean of the error of the model without gradients (Figure 7D). The values in **Figure 8D** were fitted with cubic spline interpolation using the logarithm of the number of GCs as abscissa.

To quantify the transition time between two target frequencies of the PC, the spike histogram was fitted with the equation

$$f(t) = 80 + \frac{-80 + 40}{1 + e^{-(t-200)/t_T}} + \frac{-40 + 120}{1 + e^{-(t-300)/t_T}}$$

where f is the spike frequency in Hz and t the time in ms. The transition time t_T corresponds to the 23% to 77% decay and rise time for the transition from 80 to 40 Hz and from 40 to 120 Hz, respectively.

Sensitivity of model parameters

We verified that our conclusions do not critically depend on specific parameters of the model. For example, decreasing the simulation time interval from 1 ms to 100 µs, resulted in difference of the best van Rossum error of 21% between models with and without gradients consisting of 100 GC, compared with a difference of 17% between the corresponding models with the default simulation time interval of 1 ms (cf. **Figure 8D**). With 4 MFs per GCs (not 2) the difference of the best van Rossum error was 15% between models with and without gradients consisting of 100 GC (17% with 2 MF per GC). With a membrane resistance of the PC of 100 MΩ (not 15 MΩ) the difference of the best van Rossum error was 23% between models with and without gradients consisting of 100 GC (17% with 15 MΩ). Finally, changing the target sequence to 80, 0, and 120 Hz (not 80, 40, and 120 Hz) resulted in very similar results as obtained with the original target (compare Figure **Figure 8C-E** with **Figure 8—figure supplement 1 H-J** and **Figure 8—figure supplement 1 D-F with Figure 8—figure supplement 1 K-M**).

Statistical testing

All data are expressed as mean ± SEM. The number of analyzed cells is indicated in the figures. To test for statistically significant differences of normally

873 distributed data, we performed ANOVA or Student's t-tests and provided the P
874 value ($P_{ANOVA,}$ and $P_{T\text{-}TEST}$, respectively) above the bar-graphs. To test the
875 differences between single groups we performed a Tukey post-hoc test and
876 provided the corresponding P value in the figure legend (P_{Tukey}). For not normally
877 distributed data we performed a Mann-Whitney test.
878

Figures and figure legends:

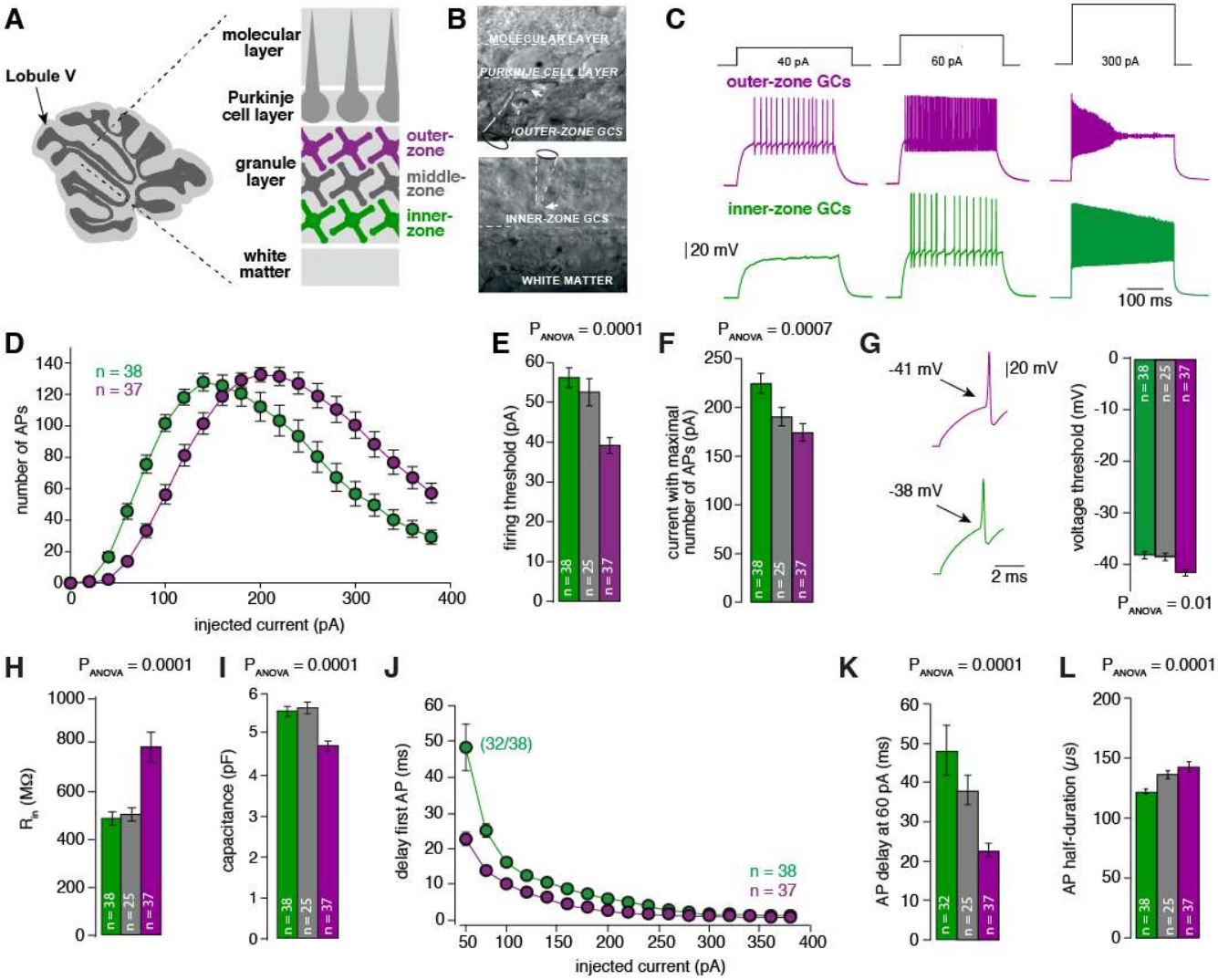

Figure 1: **A gradient in the biophysical properties of inner- to outer-zone GCs**

A. Scheme of a parasagittal slice from the cerebellar cortex were lobule V is indicated by an arrow. Enlargement shows a schematic representation of the white matter, the GC, PC and molecular layer of the cerebellar cortex. Throughout the manuscript, inner-zone GCs (close to the white matter) are depicted in green, the middle-zone GCs in grey, and the outer-zone GC (close to the PCs) in magenta.

B. Example differential-interference-contrast (DIC) microscopic images of acute cerebellar slices during recordings from outer- (top) and an inner-zone GCs (bottom). The pipette is indicated with dashed line.

C. Example current-clamp recordings from an outer-zone GC (magenta, top) and an inner-zone GC (green, bottom) after injection of increasing currents (40 pA, 60 pA and 300 pA).

D. Number of action potentials from inner- (green, n = 38) and outer- (magenta, n = 37) zone GCs plotted against the injected current. Note that the maximum number of action potentials is similar but outer-zone GCs achieved the maximum firing rate with a lower current injection.

E. Average current threshold for action potential firing of inner- (green), middle- (grey) and outer-zone GCs (right) (P_{Tukey} = 0.0001 for inner- vs outer-zone GCs).

F. Average current needed to elicit the most number of action potentials for of inner- (green), middle- (grey) and outer-zone GCs (magenta) (P_{Tukey} = 0.0005 for inner- vs outer-zone GCs).

G. Left: example action potentials from an inner- and outer-zone GC with the indicated (arrows) mean voltage-threshold for firing action potentials. Right: Comparison of the average voltage threshold for action potential firing (P_{Tukey} = 0.002 for inner- vs outer-zone GCs).

H. Average input resistance of inner- (green), middle- (grey) and outer-zone GCs (P_{Tukey} = 0.0001 for inner- vs outer-zone GCs).

I. Average capacitance of inner-, middle- and outer-zone GCs (P_{Tukey} = 0.0001 for inner- vs outer-zone GCs).

J. Delay time of the first action potential plotted against the injected current. Note, only 32 of 38 inner-zone GCs were firing action potential at a current injection of 60 pA.

K. Delay of the first action potential of inner- (green), middle- (grey) and outer-zone GCs at a current injection of 60 pA (P_{Tukey} = 0.0001 for inner- vs outer-zone GCs).

L. Average action potential half-duration of inner- (green), middle- (grey) and outer-zone GCs (P_{Tukey} = 0.0001 for inner- vs outer-zone GCs).

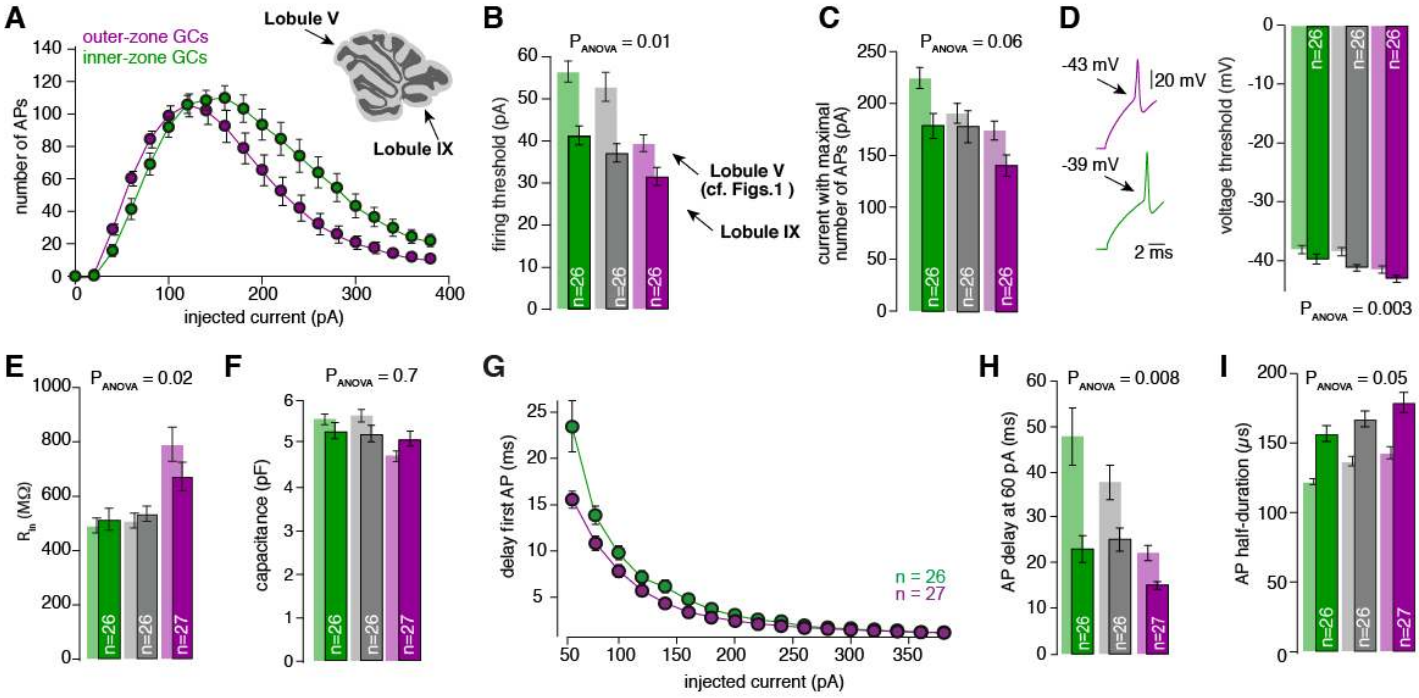

Figure 1—figure supplement 1: The gradient in the biophysical properties of GCs and PFs is preserved throughout the cerebellar cortex.

A. Number of action potentials (APs) from inner (green) and outer (magenta) zone GCs plotted against the injected current. The maximum number of action potentials is similar but with more current injection, inner-zone GCs fire more action potentials. Inset: An image of a cerebellar slice shows were the lobule V and lobule IX are indicated by arrows.

B. Bar graphs represent the firing threshold of GCs from inner (dark-green), middle (dark-grey) and outer-zone (dark-magenta). The light-colored bar graphs in the background are the data from lobule V shown in Figure 1. Firing threshold is higher in inner- compared to outer-zone GCs from lobule IX, and with the same current injection, GCs from lobule IX fire action potentials faster compared to lobule V. The numbers of recorded GCs for lobule IX (n) are indicated (P_{Tukey} = 0.007 for inner- vs outer-zone GCs).

C. Average current needed to elicit the maximum number of action potentials for of inner- (green), middle- (grey) and outer-zone GCs (magenta) (P_{Tukey} = 0.002 for inner- vs outer-zone GCs).

D. Left: example action potentials from an inner- and outer-zone GC with the indicated (arrows) mean voltage threshold for firing action

potentials. Right: Voltage threshold to elicit action potentials in inner-, middle- and outer-zone GCs from lobule IX compared with data from lobule V. Voltage threshold for outer-zone GCs is lower compared to inner-zone GCs from lobule IX (P_{Tukey} = 0.002 for inner- vs outer-zone GCs).

E. Input resistance of GCs from outer-zone of lobule IV is higher compared to inner- and middle zone GCs. But there is no difference between the input resistance of GCs from lobule V and IX (P_{Tukey} = 0.02 for inner- vs outer-zone GCs).

F. Average capacitance of inner-, middle- and outer-zone GCs. In contrary to lobule V there is no difference in the capacitance of GC from inner-, middle, or outer-zone (P_{Tukey} = 0.7 for inner- vs outer-zone GCs).

G. Delay of the first action potential plotted against the injected current.

H. Delay of the first action potential after a current injection of 60 pA from inner-, middle- and outer-zone GCs from lobule IX compared to lobule V (P_{Tukey} = 0.05 for inner- vs outer-zone GCs).

I. The action potential half-duration of inner-zone (dark-green) GCs from lobule IX is shorter compared to middle (dark-grey)- and outer-zone (dark-magenta) GCs. Compared to lobule V (faded-green, faded grey and faded magenta), the GCs from lobule IX showed a broader action potential half-width (P_{Tukey} = 0.09 for inner- vs outer-zone GCs).

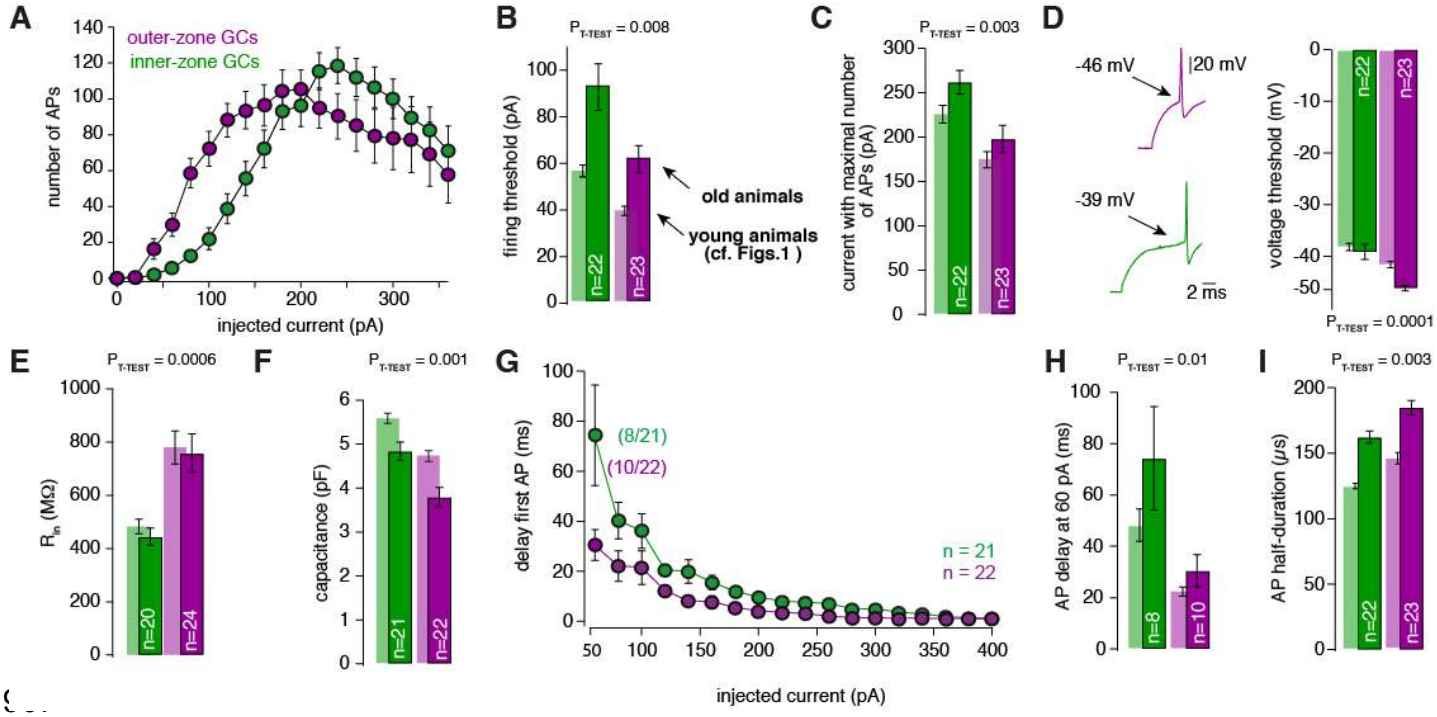

968 **Figure 1—figure supplement 2: The gradient in the biophysical properties**
969 **of GCs and PFs is also found in 3-month-old animals.**

970 A. Number of action potentials (APs) from inner (green) and outer
971 (magenta) zone GCs plotted against the injected current. The
972 maximum number of action potentials is similar, but with more current
973 injection, inner-zone GCs fire more action potentials. For all the
974 measurements GCs from lobule V were used.
975 B. Bar graphs represent the firing threshold of GCs from inner (dark-
976 green), and outer-zone (dark-magenta). The light-colored bar graphs
977 in the background are the data from lobule V in young (21-30 days-
978 old) animals shown in Figure 1. Firing threshold is higher in inner -
979 compared to outer-zone GCs from old animals.
980 C. Average current needed to elicit the maximum number of action
981 potentials for of inner- (green), and outer-zone GCs (magenta).
982 D. Left: example action potentials from an inner- and outer-zone GC with
983 the indicated (arrows) mean voltage-threshold for firing action
984 potentials. Right: voltage threshold to elicit action potentials in inner-,
985 middle- and outer-zone GCs from old animals compared with data
986 from young animals.
987 E. Input resistance of GCs from outer-zone is higher compared to inner-
988 zone GCs. But there is no difference between the input resistance of
989 GCs from young and old animals.

F. Average capacitance of inner- and outer-zone GCs. In agreement with the data from the young animals, inner-zone GCs have a higher capacitance compered to outer-zone GCs.

G. Delay of the first action potential plotted against the injected current. Since the mean current threshold is higher compared to young animals only 8 out of 21 GCs from inner- and 10 out of 22 GCs from outer-zone already fired action potentials at a current injection

H. Delay of the first action potential after a current injection of 60 pA from inner-, middle- and outer-zone GCs from lobule IX compared to lobule V.

I. The action potential half-duration of inner-zone (dark-green) GCs from old animals is shorter compared with outer-zone (dark-magenta) GCs.

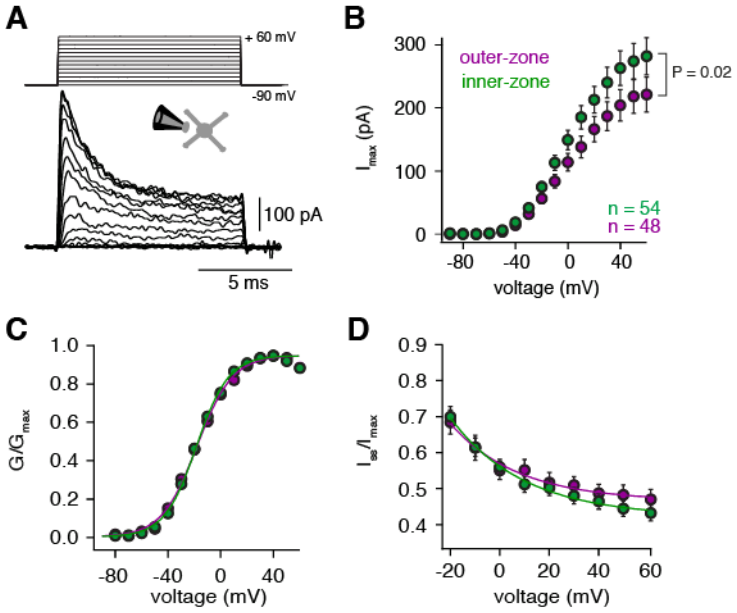

Figure 2: Voltage-gated potassium currents are larger at inner-zone GCs

A. Example potassium currents from outside-out patches of cerebellar GCs evoked by voltage steps from -90 to +60 mV in 10 mV increments with a duration of 10 ms. All recordings were made in the presence of 1 µM TTX and 150 µM $CdCl_2$ to block voltage-gated sodium and calcium channels, respectively.

B. Average peak potassium current (I_{max}) plotted versus step potential of inner (green) and outer-zone (magenta) GCs. Significance level was tested with a Mann-Whitney Test and the P value is indicated in the figure. Note, that the P value shows the significance level at 60 mV.

C. Average normalized peak potassium conductance (G/G_{max}) versus step potential of inner (green) and outer-zone (magenta) GCs.

D. Average steady-state current (I_{ss}, mean current of the last 2 ms of the 10ms depolarization) normalized to the peak current (I_{max}) versus step potential of inner (green) and outer-zone (magenta) GCs.

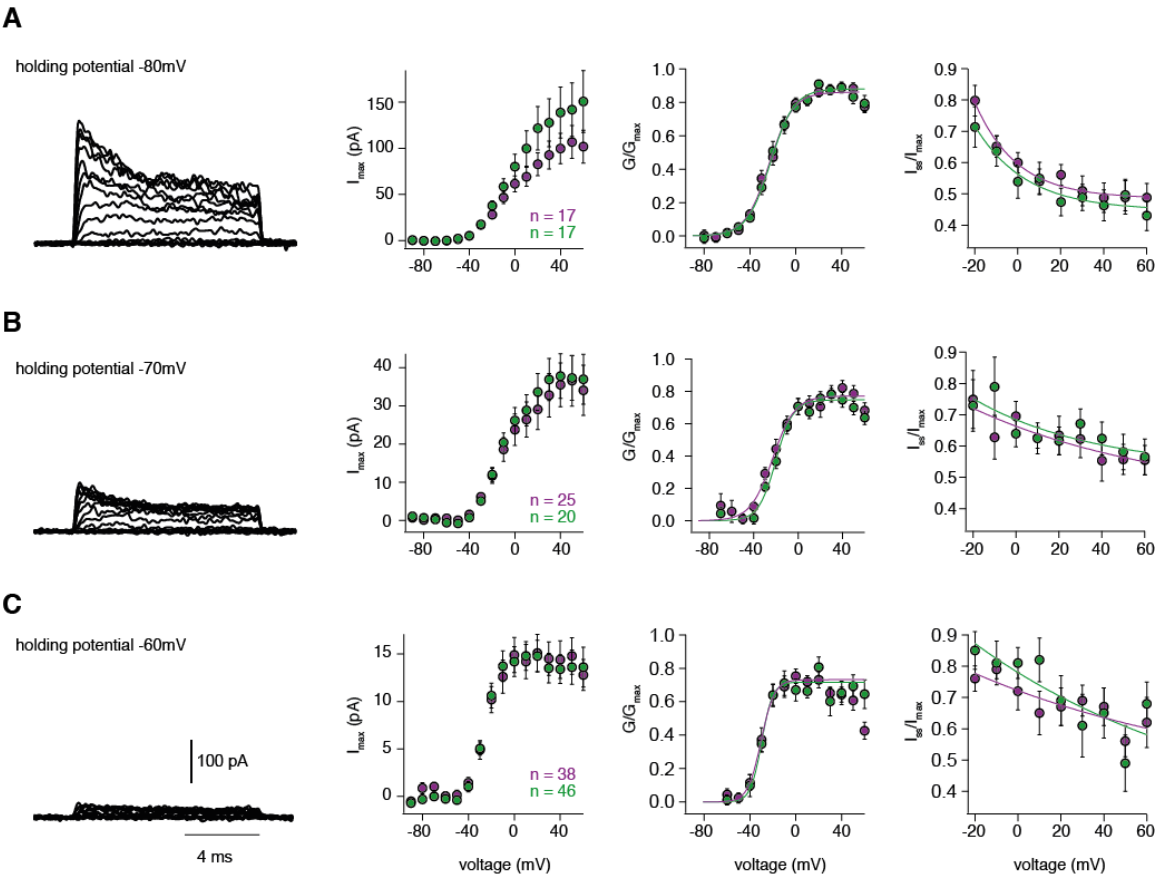

Figure 2—figure supplement 1: Steady-state activation and inactivation are similar for inner and outer GCs.

A – C left: Example potassium currents from outside-out patches of cerebellar GCs evoked by voltage steps from -90 to +60 mV in 10 mV increments with a duration of 10 ms. The intersweep holding potential varied between -80 mV (**A**), -70 mV (**B**) and -60 mV (**C**). Panels show the corresponding current-voltage relationship (first panel) of inner-zone (green) and outer-zone (magenta) GCs, the normalized conductance (second panel) and the normalized inactivation behavior (third panel). The number of measured cells are indicated in the figure.

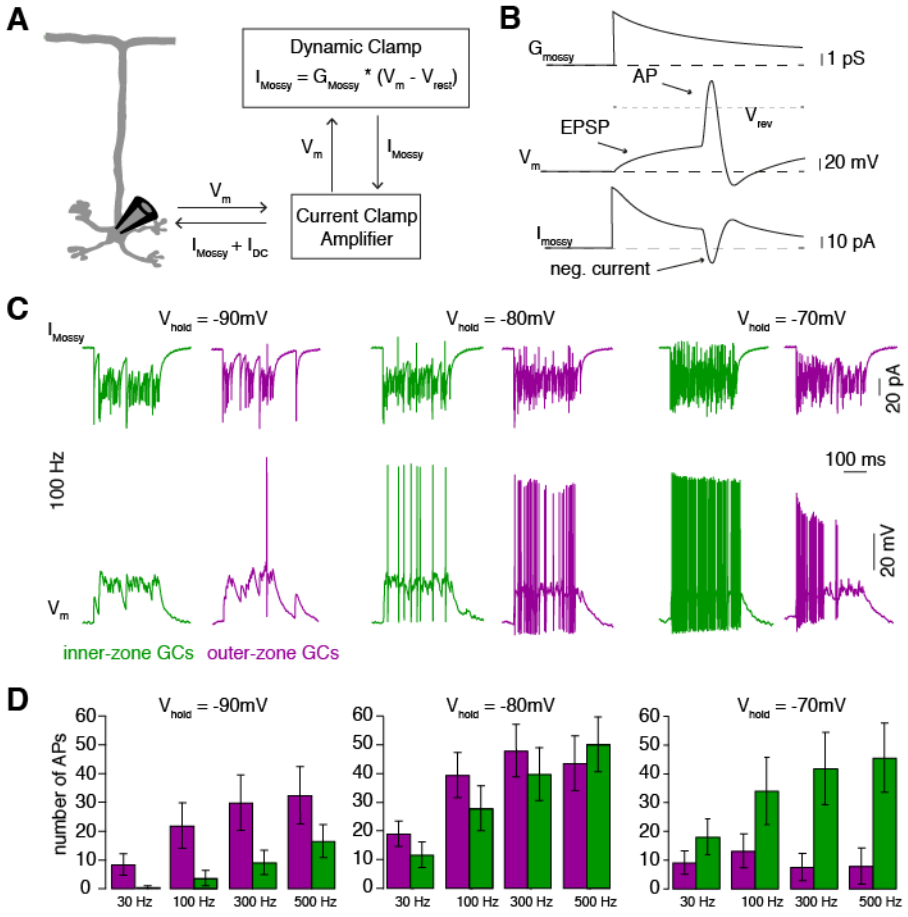

Figure 3: MF inputs are differentially processed by inner and outer GCs

A. Schematic representation of the Dynamic Clamp system.

B. Illustration of MF conductance (G_{mossy}), GC membrane potential (V_m), and MF current (I_{mossy}) for the dynamic clamp technique. Note the prediction of a negative current during the action potential as apparent in the experimental traces in panel C.

C. Example dynamic clamp recordings of inner- (green) and outer-zone (magenta) GCs at different holding potentials (-90 mV left; -80 mV middle and -70 mV right) at a stimulation frequency of 100 Hz. Upper trace represents the poisson-distributed MF-like EPSCs. Lower trace shows the measured EPSPs and action potentials.

D. Average number of measured action potentials (APs) after mossy-fiber like EPSC injection at different frequencies and the indicated holding potentials.

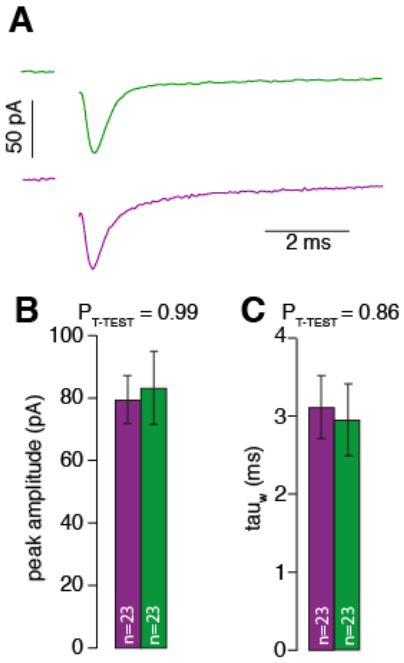

Figure 3—figure supplement 1: MF input is similar for inner- and outer-zone GCs.

A. Examples of single EPSCs measured from inner- (green) and outer-zone GCs (magenta) after 1Hz stimulation of MF axons. Stimulation artifacts were removed.

B. Average amplitude of EPSCs from inner- (green) and outer-zone GCs.

C. Weighted decay time (see material and methods) of EPSCs from inner- (green) and outer-zone (magenta).

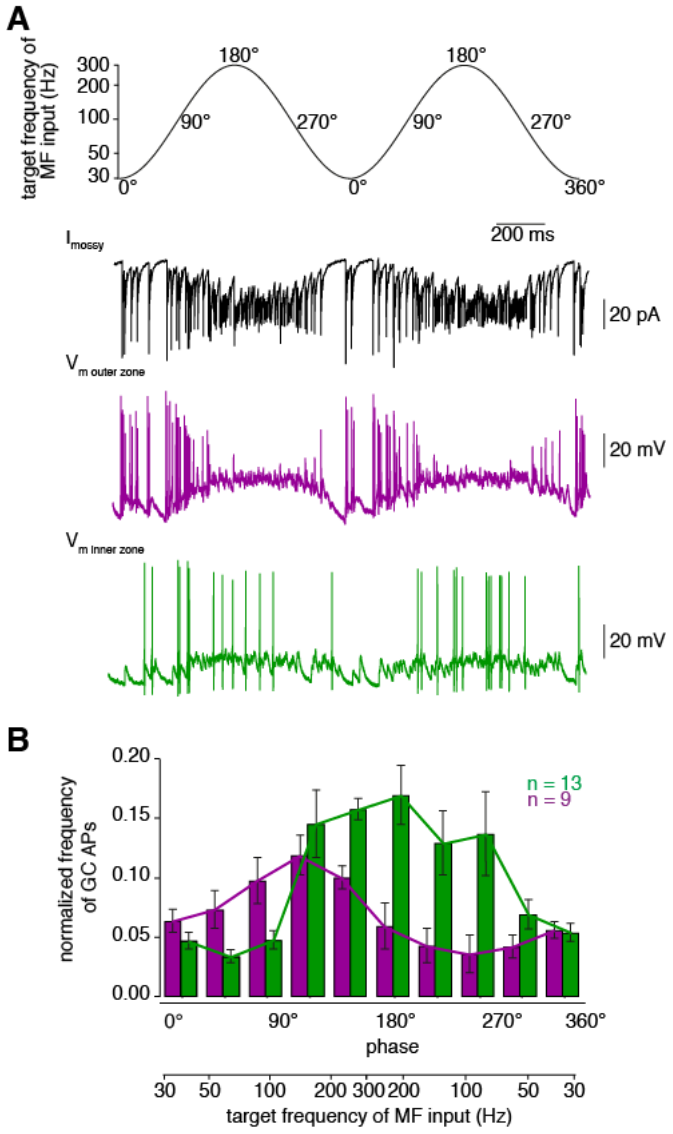

Figure 4: Fourier-like transformation of MF input frequency

A Target frequency of the dynamic clamp MF-like sinusoidal EPSC input current. The frequencies ranged from 30 to 300 Hz and the duration was 1s. The degree values denote the phase angle. *Black:* example trace of poisson-distributed MF-like input current. *Magenta and green:* Dynamic clamp measurement of outer- and inner-zone GCs, respectively, after stimulation with a MF-like current shown in black at a holding potential of approximately -70 mV.

B Histogram of the normalized frequency of action potentials (APS) fired by GCs at different time intervals during 1s stimulation with poisson-distributed MF-like currents shown in A. Each bar represents a time window of 100 ms. Green: inner-zone GCs, magenta: outer-zone GCs.

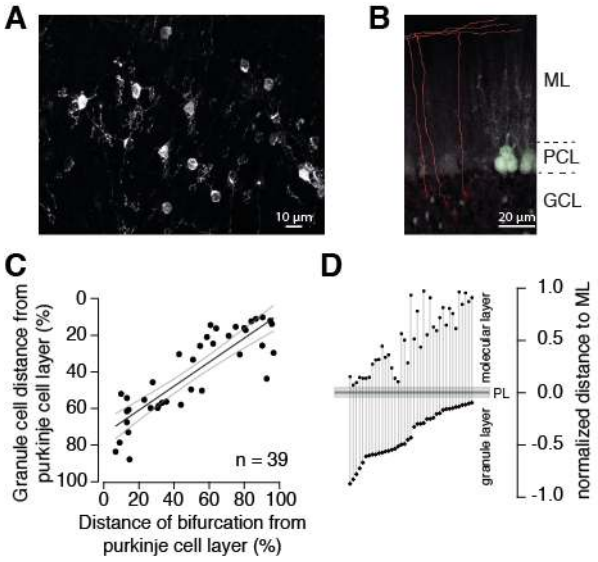

Figure 5: The position of PFs is correlated with the position of GC somata

A. Example of GCs labeled with DiI 24 h post injection. Numerous GCs from inner-, middle-, and outer-zone were labeled.

B. Example of traced axons from different GCs from the outer zone. The axon was traced (red) from the cell soma to the bifurcation side in the molecular layer. Stained cell bodies of PFs are also visible (white). *ML:* molecular layer; *PCL:* Purkinje cell layer; *GCL:* granule cell layer.

C. The distance between labeled GCs and the PC layer strongly correlated with the distance between the axon bifurcation and the PC layer (Pearson's correlation coefficient r = -0.862; p<0.001). Solid black line depicts the linear interpolation and the grey lines represent SEM of the fit. The number of recorded GCs (n) is indicated.

D. Position of the GC somata from the granular layer of each traced cell linked to the position of the bifurcation side in the molecular layer. To avoid variability, all the distances were normalized to the corresponding molecular layer hight.

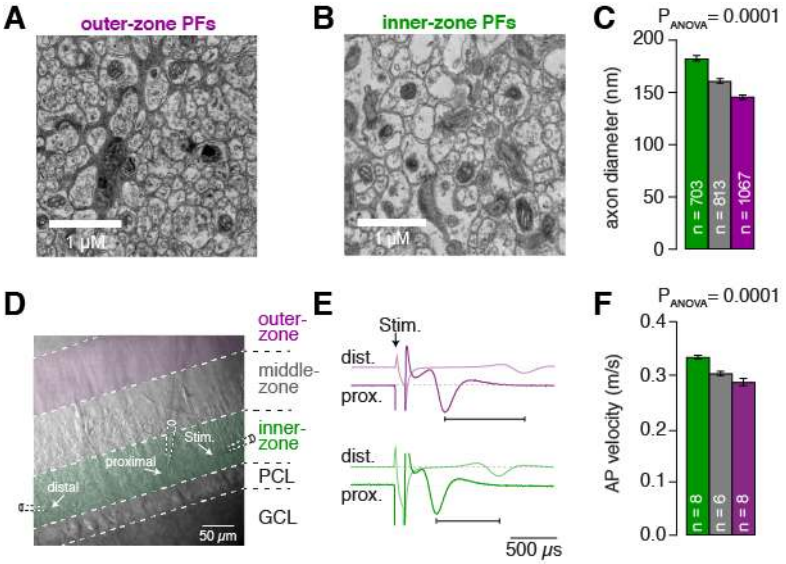

Figure 6: Inner-zone PFs have larger diameter and higher action potential propagation velocity.

A. Electron microscopic image of the outer (A) and inner zone (B) of sagittal sections through the molecular layer.
C. Summary of axon diameters in the inner (green), middle (grey), and outer zone (magenta) of the molecular layer (P_{Tukey} = 0.0001 for inner- vs outer-zone GCs).
D. DIC image of the molecular layer superimposed with a schematic illustration of the experimental setup to measure compound action potentials from PFs. Compound action potentials were evoked by a stimulus electrode (left) and recorded by a proximal and distal recording electrode (middle, right).
E. Example traces used to determine the conduction velocity between inner-, middle-, and outer-zone PFs. The time difference between the compound action potential arriving at the proximal electrode (solid traces) and the distal electrode (faint traces) was used to determine the velocity. The time was shorter for inner-zone PFs (green) compared with outer-zone PFs (magenta).
F. Summary of action potential (AP) velocity in inner-, middle- and outer-zones (P_{Tukey} = 0.0001 for inner- vs outer-zone GCs).

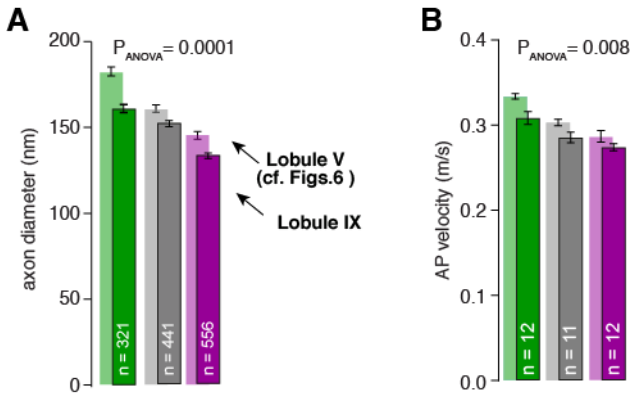

Figure 6—figure supplement 1: Differences in axon diameter and action potential velocity are also found in lobule IX.

A. Summary of axon diameters in the inner (green), middle (grey), and outer zone (magenta) of the molecular layer (P_{Tukey} = 0.0001 for inner- vs outer-zone GCs). The light-colored bar graphs in the background are the data from lobule V shown in Figure 6.

B. Summary of action potential (AP) velocity in inner-, middle- and outer-zones of PF from molecular layer of lobule IX (P_{Tukey} = 0.0001 for inner- vs outer-zone GCs).

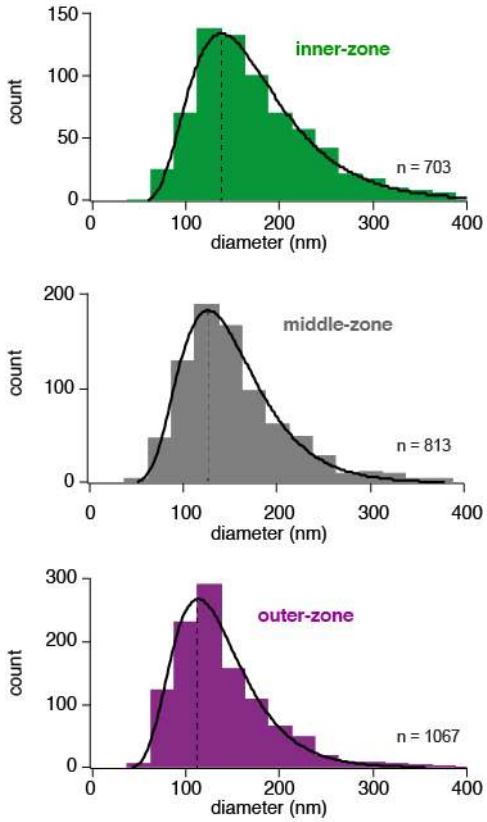

Figure 6—figure supplement 2: Histogram of the axon diameters.

Histograms of the diameter of inner-, middle- and outer-zone axons in the molecular layer, indicating that the change in axon diameter is not due to an increased fraction of larger diameter axons from non-GC cells (e.g. Lugaro cells). Instead the entire distribution of the axon diameters is shifted between zones.

Data were fit with a skewed Gaussian function: $a\, e^{\left[-\log(2)\left(\left(log\left(1+2b\frac{d-d0}{ds}\right)/b\right)^2\right)\right]}$, where *a* is the amplitude, *d* the diameter, and *d0* the diameter at the peak. *ds* and *b* represent parameters related to the width and the skewness, respectively. The peak is indicated by a vertical line.

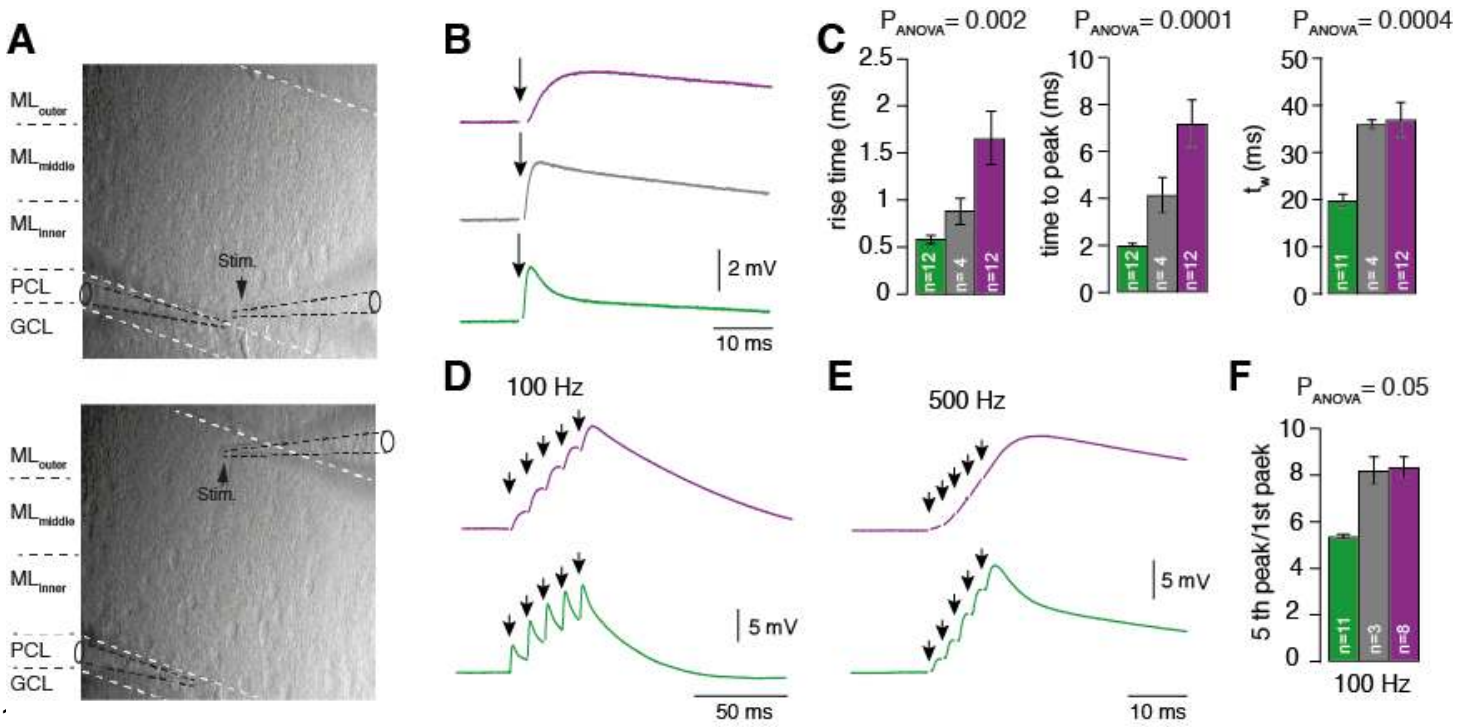

Figure 7: PCs process inner-, middle-, and outer-zone PF inputs differentially

A. DIC image of the molecular layer superimposed with a schematic illustration of PC recordings while stimulating inner (top) and outer-zone PFs (bottom). Shown are the GC layer (GL), PC layer (PC) and molecular layer (ML).

B. EPSPs measured at the PC soma after stimulation (1 Hz) of inner- (green), middle- (grey), and outer-zone PFs (magenta).

C. Average 20% to 80% rise time, time to peak and weighted time-constant of PC EPSPs after stimulation of inner- (green; n = 12), middle- (grey; n = 4) and outer-zone PFs (magenta; n = 12) as shown in B (P_{Tukey} = 0.001; P_{Tukey} = 0.0001; P_{Tukey} = 0.0004 for inner- vs outer-zone GCs, respectively).

D-E. Example traces of EPSPs from a PC after five impulses to inner- (green) and outer-zone PFs (magenta) at 100 Hz (D) and 500 Hz (E).

F. Average paired-pulse ratio measured in PCs after five 100-Hz stimuli at inner- (green; n = 11), middle- (grey, n = 3) and outer- zone PFs (magenta, n = 8) (P_{Tukey} = 0.054 for inner- vs outer-zone GCs).

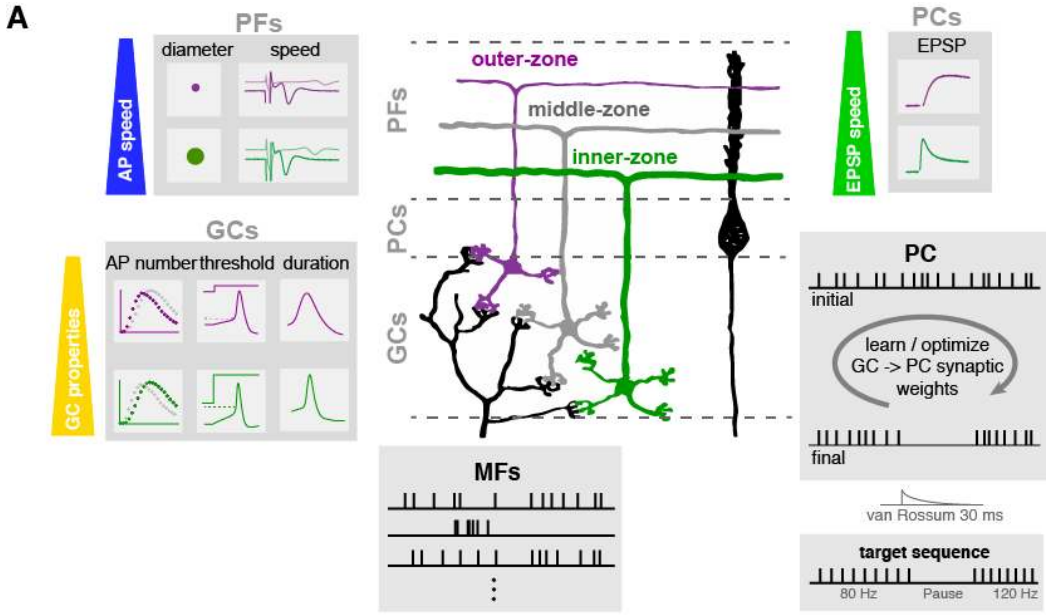

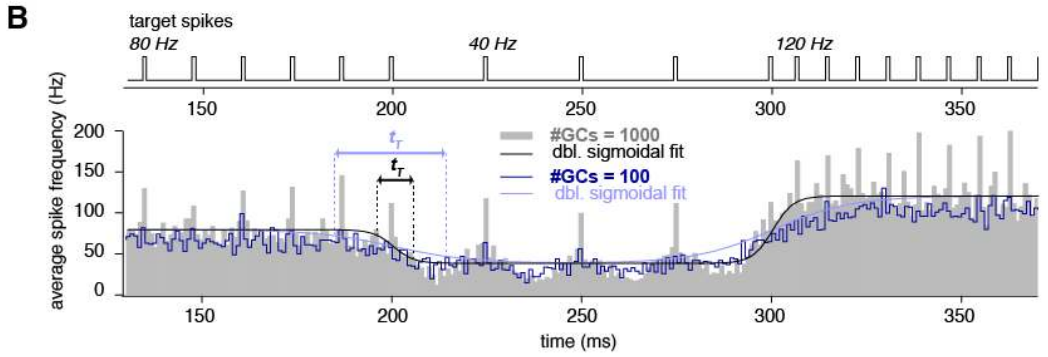

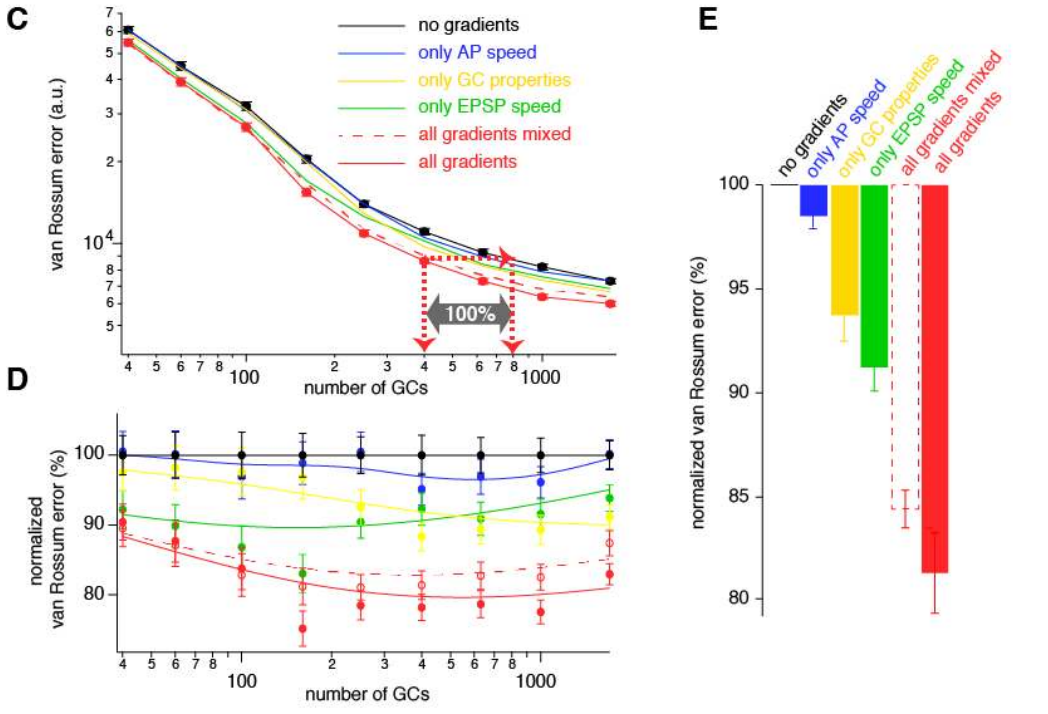

Figure 8: The observed neuronal gradients increase storing capacity and improve temporal precision of PC spiking

A. Schematic illustration of the network model of the cerebellar cortex as explained in the main text.

B. Average spiking histogram for models consisting of 100 and 1000 GCs, superimposed with double sigmoidal fits constrained to 80, 40 and 120 Hz. Above the target spiking sequence is indicated. t_T indicates the transition time of the sigmoidal fit for the respective number of GCs.

C. Double logarithmic plot of the average minimal van Rossum error plotted against the number of GCs for a model with no gradients (black), a model with only gradually varied GC parameters (yellow), PF propagation speed (blue), EPSP kinetics (green), and all gradients (red). Furthermore, all parameters were gradually varied but the connectivity between GC, PF and EPSPs was random (all gradients mixed; dashed red). Red dashed lines with arrows indicate the number of GCs needed to obtain the same van Rossum error with all gradients compared to no gradients. With no gradients 100% more GCs are needed to obtain the same van Rossum error.

D. Average van Rossum errors as shown in panel C but normalized to the value of the model without gradients, superimposed with a smoothing spline interpolation.

E. Error bar indicate average of the relative differences shown in panel D.

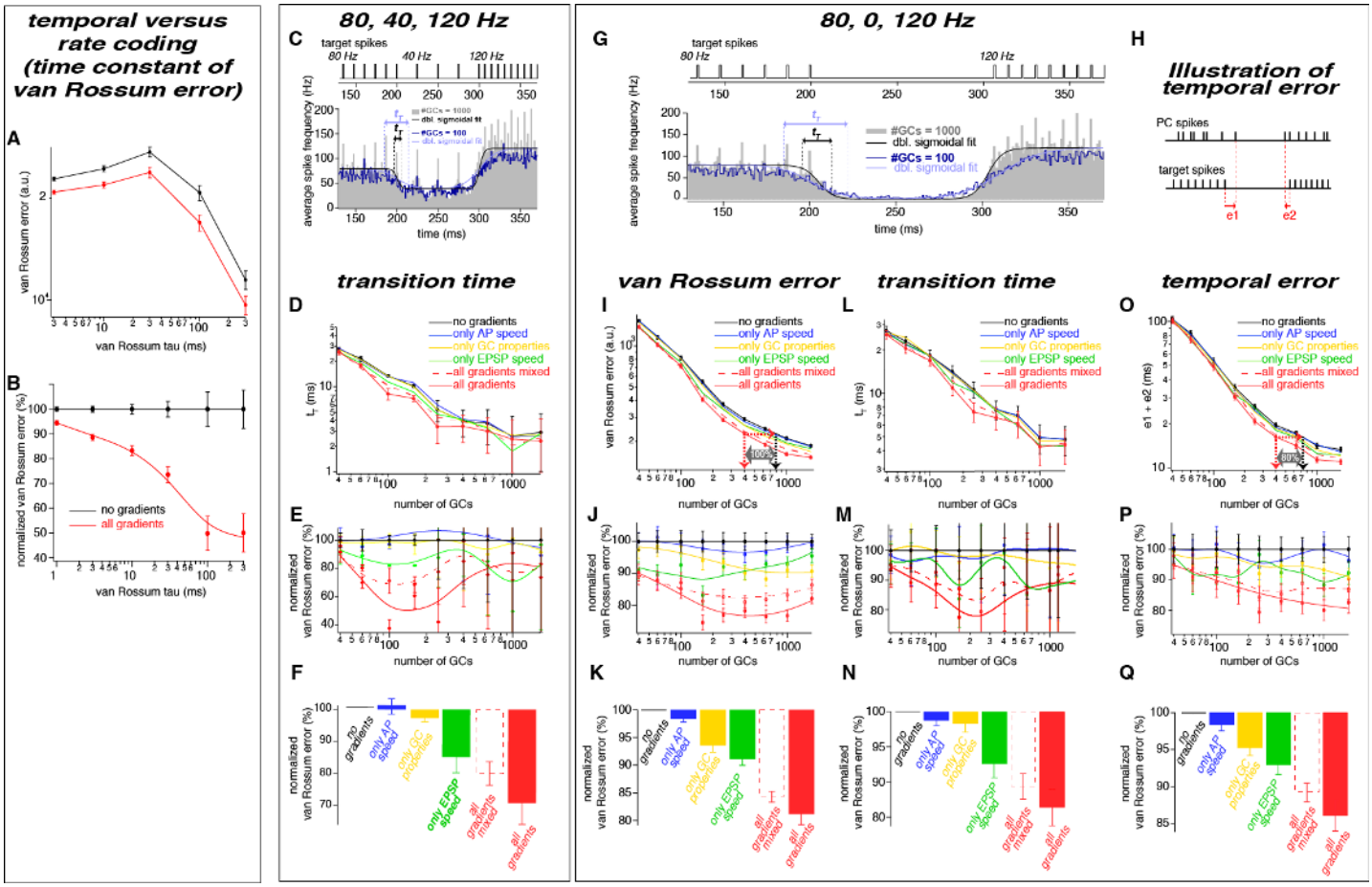

Figure 8—figure supplement 1: The observed neuronal gradients reduce the temporal error and improve rate coding of PC spikes.

A. Double logarithmic plot of the van Rossum error of model with 300 GCs without (black) and with all gradients (red) plotted versus the time constant of the van Rossum kernel ranging from 2 to 300 ms.

B. Data as in panel A normalized to the model without gradients.

C. Average spiking histogram for models consisting of 100 and 1000 GCs, superimposed with double sigmoidal fits constrained to 80, 40 and 120 Hz. Above the target spiking sequence is indicated.

D. Double logarithmic plot of the transition time (t_T) of the double exponential fits as illustrated in panel C. Error bars represent 95% confidence intervals.

E. Transition time (t_T) as shown in panel D but normalized to the value of the model without gradients, superimposed with a smoothing spline interpolation.

F. Average of the relative differences shown in panel E.

G. Average spiking histogram for models consisting of 100 and 1000 GCs, superimposed with double sigmoidal fits constrained to 80, 0 and

120 Hz. Above the target spiking sequence with 80, 0, and 120 Hz is indicated.

H. Illustration of the temporal error (e1 and e2) of the spikes defining the beginning and the end of the pause.

I-K, L-N, and O-Q. Same plots as D-F but for the 80, 0, 120 Hz target sequence and the van Rossum error (I-K), the transition time (t_T) (L-N) and the temporal errot (O-Q).

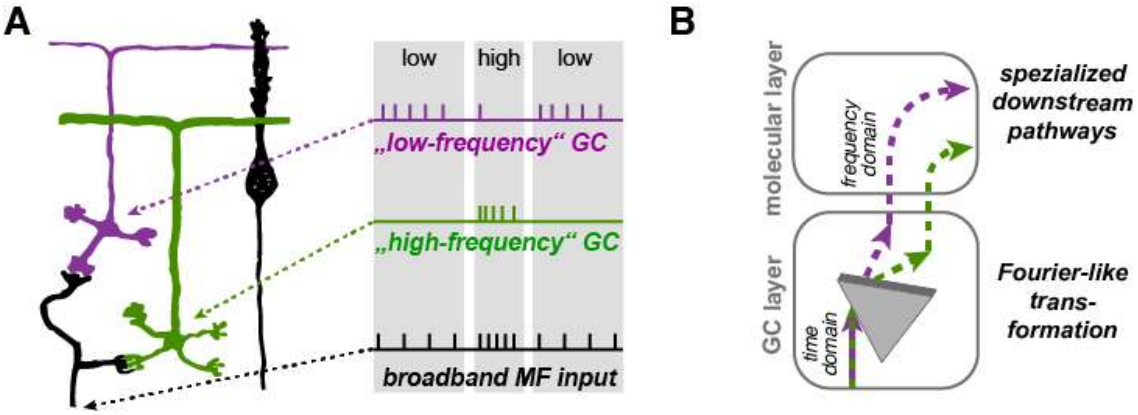

Figure 9: Illustration of the concept of Fourier-like transformation in the cerebellar cortex

A. Illustration of a broadband MF inputs conveying a sequence of low, high, and low firing frequency. Inner-zone GCs will preferentially fire during high-frequency inputs ('high-frequency' GC) and outer-zone GCs during low-frequency inputs ('low-frequency' GC).

B. Schematic illustration of the signal flow through the cerebellar cortex. The Fourier-like transformation in the GC layer is illustrated as an optical prism separating the spectral components on the MF input. Thereby the MF signal in the time domain is transformed to the frequency domain and sent via specialized signaling pathways in the molecular layer to the PC.

References

Albergaria, C., Silva, N.T., Pritchett, D.L., and Carey, M.R. (2018). Locomotor activity modulates associative learning in mouse cerebellum. Nat Neurosci 21, 725-735.

Albus, J.S. (1971). A Theory of Cerebellar Function. Math Biosci 10, 25–61.

Apps, R., Hawkes, R., Aoki, S., Bengtsson, F., Brown, A.M., Chen, G., Ebner, T.J., Isope, P., Jörntell, H., Lackey, E.P., *et al.* (2018). Cerebellar modules and their role as operational cerebellar processing units. The Cerebellum 17, 654-682.

Arenz, A., Silver, R.A., Schaefer, A.T., and Margrie, T.W. (2008). The contribution of single synapses to sensory representation in vivo. Science 321, 977-980.

Baade, C., Byczkowicz, N., and Hallermann, S. (2016). NMDA receptors amplify mossy fiber synaptic inputs at frequencies up to at least 750 Hz in cerebellar granule cells. Synapse 70, 269-276.

Babadi, B., and Sompolinsky, H. (2014). Sparseness and expansion in sensory representations. Neuron 83, 1213-1226.

Baginskas, A., Palani, D., Chiu, K., and Raastad, M. (2009). The H-current secures action potential transmission at high frequencies in rat cerebellar parallel fibers. Eur J Neurosci 29, 87-96.

Barbour, B. (1993). Synaptic currents evoked in Purkinje cells by stimulating individual granule cells. Neuron 11, 759-769.

Bengtsson, F., and Jörntell, H. (2009). Sensory transmission in cerebellar granule cells relies on similarly coded mossy fiber inputs. Proc Natl Acad Sci U S A 106, 2389.

Billings, G., Piasini, E., Lőrincz, A., Nusser, Z., and Silver, R.A. (2014). Network structure within the cerebellar input layer enables lossless sparse encoding. Neuron 83, 960–974.

Blot, A., and Barbour, B. (2014). Ultra-rapid axon-axon ephaptic inhibition of cerebellar Purkinje cells by the pinceau. Nat Neurosci 17, 289-295.

Blot, A., de Solages, C., Ostojic, S., Szapiro, G., Hakim, V., and Lena, C. (2016). Time-invariant feed-forward inhibition of Purkinje cells in the cerebellar cortex in vivo. J Physiol 594, 2729-2749.

Braitenberg, V., Heck, D., and Sultan, F. (1997). The detection and generation of sequences as a key to cerebellar function: Experiments and theory. Behav Brain Sci 20, 229-&.

Brown, S.T., and Raman, I.M. (2018). Sensorimotor Integration and Amplification of Reflexive Whisking by Well-Timed Spiking in the Cerebellar Corticonuclear Circuit. Neuron 99, 564-575 e562.

Brunel, N., Hakim, V., Isope, P., Nadal, J.P., and Barbour, B. (2004). Optimal information storage and the distribution of synaptic weights: perceptron versus Purkinje cell. Neuron 43, 745-757.

Cayco-Gajic, N.A., Clopath, C., and Silver, R.A. (2017). Sparse synaptic connectivity is required for decorrelation and pattern separation in feedforward networks. Nat Commun 8, 1116.

Cayco-Gajic, N.A., and Silver, R.A. (2019). Re-evaluating Circuit Mechanisms Underlying Pattern Separation. Neuron 101, 584-602.

1273 Cembrowski, M.S., and Spruston, N. (2019). Heterogeneity within classical cell types
1274 is the rule: lessons from hippocampal pyramidal neurons. Nat Rev Neurosci 20,
1275 193-204.
1276 Chabrol, F.P., Arenz, A., Wiechert, M.T., Margrie, T.W., and DiGregorio, D.A. (2015).
1277 Synaptic diversity enables temporal coding of coincident multisensory inputs in
1278 single neurons. Nat Neurosci 18, 718-727.
1279 Chadderton, P., Margrie, T.W., and Häusser, M. (2004). Integration of quanta in
1280 cerebellar granule cells during sensory processing. Nature 428, 856-860.
1281 Clopath, C., and Brunel, N. (2013). Optimal properties of analog perceptrons with
1282 excitatory weights. PLoS Comput Biol 9, e1002919.
1283 Clopath, C., Nadal, J.P., and Brunel, N. (2012). Storage of correlated patterns in
1284 standard and bistable Purkinje cell models. PLoS Comput Biol 8, e1002448.
1285 D'Angelo, E., Rossi, P., and Taglietti, V. (1993). Different proportions of N-methyl-D-
1286 aspartate and non-N-methyl-D-aspartate receptor currents at the mossy fibre-
1287 granule cell synapse of developing rat cerebellum. Neuroscience 53, 121-130.
1288 De Schutter, E., and Bower, J.M. (1994a). An active membrane model of the
1289 cerebellar Purkinje cell II. Simulation of synaptic responses. J Neurophysiol 71,
1290 401-419.
1291 De Schutter, E., and Bower, J.M. (1994b). An active membrane model of the
1292 cerebellar Purkinje cell. I. Simulation of current clamps in slice. J Neurophysiol
1293 71, 375-400.
1294 De Schutter, E., and Bower, J.M. (1994c). Simulated responses of cerebellar Purkinje
1295 cells are independent of the dendritic location of granule cell synaptic inputs.
1296 Proc Natl Acad Sci U S A 91, 4736-4740.
1297 Dean, D., Porrill, J., Ekerot, C.F., and Jörntell, H. (2010). The cerebellar microcircuit as
1298 an adaptive filter: experimental and computational evidence. Nat Neurosci 11,
1299 30-43.
1300 Delvendahl, I., Straub, I., and Hallermann, S. (2015). Dendritic patch-clamp
1301 recordings from cerebellar granule cells demonstrate electrotonic compactness.
1302 Front Cell Neurosci 9.
1303 Desai, N.S., Gray, R., and Johnston, D. (2017). A Dynamic Clamp on Every Rig. eNeuro
1304 4.
1305 Dhar, M., Hantman, A.W., and Nishiyama, H. (2018). Developmental pattern and
1306 structural factors of dendritic survival in cerebellar granule cells in vivo. Sci Rep
1307 8, 17561.
1308 Dieudonne, S., and Dumoulin, A. (2000). Serotonin-driven long-range inhibitory
1309 connections in the cerebellar cortex. J Neurosci 20, 1837-1848.
1310 Dizon, M.J., and Khodakhah, K. (2011). The role of interneurons in shaping purkinje
1311 cell responses in the cerebellar cortex. J Neurosci 31, 10463-10473.
1312 Doussau, F., Schmidt, H., Dorgans, K., Valera, A.M., Poulain, B., and Isope, P. (2017).
1313 Frequency-dependent mobilization of heterogeneous pools of synaptic vesicles
1314 shapes presynaptic plasticity. Elife 6.
1315 du Lac, S., Raymond, J.L., Sejnowski, T.J., and Lisberger, S.G. (1995). Learning and
1316 memory in the vestibulo-ocular reflex. Annu Rev Neurosci 18, 409-441.
1317 Eccles, J.C., Ito, M., and Szentagothai, J. (1967). The Cerebellum as a Neuronal
1318 Machine (Berlin: Springer-Verlag).

1319 Espinosa, J.S., and Luo, L. (2008). Timing neurogenesis and differentiation: insights
1320 from quantitative clonal analyses of cerebellar granule cells. J Neurosci 28, 2301-
1321 2312.
1322 Fletcher, L.N., and Williams, S.R. (2019). Neocortical Topology Governs the Dendritic
1323 Integrative Capacity of Layer 5 Pyramidal Neurons. Neuron 101, 76-90 e74.
1324 Fox, C.A., and Barnard, J.W. (1957). A quantitative study of the Purkinje cell
1325 dendritic branchlets and their relationship to afferent fibres. J Anat 91, 299-313.
1326 Fujita, M. (1982). Adaptive filter model of the cerebellum. Biol Cybern 45, 195-206.
1327 Gaffield, M.A., and Christie, J.M. (2017). Movement Rate Is Encoded and Influenced
1328 by Widespread, Coherent Activity of Cerebellar Molecular Layer Interneurons. J
1329 Neurosci 37, 4751-4765.
1330 Galliano, E., Gao, Z., Schonewille, M., Todorov, B., Simons, E., Pop, Andreea S.,
1331 D'Angelo, E., van den Maagdenberg, Arn M.J.M., Hoebeek, Freek E., and De Zeeuw,
1332 Chris I. (2013). Silencing the Majority of Cerebellar Granule Cells Uncovers Their
1333 Essential Role in Motor Learning and Consolidation. Cell Reports 3, 1239-1251.
1334 Gao, Z., Proietti-Onori, M., Lin, Z., Ten Brinke, M.M., Boele, H.J., Potters, J.W., Ruigrok,
1335 T.J., Hoebeek, F.E., and De Zeeuw, C.I. (2016). Excitatory Cerebellar Nucleocortical
1336 Circuit Provides Internal Amplification during Associative Conditioning. Neuron
1337 89, 645-657.
1338 Gao, Z., van Beugen, B.J., and De Zeeuw, C.I. (2012). Distributed synergistic plasticity
1339 and cerebellar learning. Nat Rev Neurosci 13, 619-635.
1340 Garrido, J.A., Ros, E., and D'Angelo, E. (2013). Spike timing regulation on the
1341 millisecond scale by distributed synaptic plasticity at the cerebellum input stage:
1342 a simulation study. Front Comput Neurosci 7, 64.
1343 Gibo, T.L., Criscimagna-Hemminger, S.E., Okamura, A.M., and Bastian, A.J. (2013).
1344 Cerebellar motor learning: are environment dynamics more important than error
1345 size? J Neurophysiol 110, 322-333.
1346 Giovannucci, A., Badura, A., Deverett, B., Najafi, F., Pereira, T.D., Gao, Z., Ozden, I.,
1347 Kloth, A.D., Pnevmatikakis, E., Paninski, L.*, et al.* (2017). Cerebellar granule cells
1348 acquire a widespread predictive feedback signal during motor learning. Nat
1349 Neurosci 20, 727-734.
1350 Guo, C., Witter, L., Rudolph, S., Elliott, H.L., Ennis, K.A., and Regehr, W.G. (2016).
1351 Purkinje Cells directly inhibit granule cells in specialized regions of the cerebellar
1352 cortex. Neuron 91, 1330-1341.
1353 Hallermann, S., Fejtova, A., Schmidt, H., Weyhersmüller, A., Silver, R.A., Gundelfinger,
1354 E., and Eilers, J. (2010). Bassoon speeds vesicle reloading at a central excitatory
1355 synapse. Neuron 18, 710-723.
1356 Harvey, R.J., and Napper, R.M. (1991). Quantitative studies on the mammalian
1357 cerebellum. Prog Neurobiol 36, 437-463.
1358 Heath, N.C., Rizwan, A.P., Engbers, J.D., Anderson, D., Zamponi, G.W., and Turner,
1359 R.W. (2014). The expression pattern of a Cav3-Kv4 complex differentially
1360 regulates spike output in cerebellar granule cells. J Neurosci 34, 8800-8812.
1361 Heiney, S.A., Wohl, M.P., Chettih, S.N., Ruffolo, L.I., and Medina, J.F. (2014).
1362 Cerebellar-dependent expression of motor learning during eyeblink conditioning
1363 in head-fixed mice. J Neurosci 34, 14845-14853.

1364 Henneman, E., Somjen, G., and Carpenter, D.O. (1965). Excitability and inhibitability
1365 of motoneurons of different sizes. J Neurophysiol 28, 599-620.
1366 Herculano-Houzel, S. (2009). The human brain in numbers: a linearly scaled-up
1367 primate brain. Front Hum Neurosci 3, 31.
1368 Herzfeld, D.J., Kojima, Y., Soetedjo, R., and Shadmehr, R. (2015). Encoding of action
1369 by the Purkinje cells of the cerebellum. Nature 526, 439-442.
1370 Hewitt, A.L., Popa, L.S., Pasalar, S., Hendrix, C.M., and Ebner, T.J. (2011).
1371 Representation of limb kinematics in Purkinje cell simple spike discharge is
1372 conserved across multiple tasks. J Neurophysiol 106, 2232-2247.
1373 Hong, S., Negrello, M., Junker, M., Smilgin, A., Thier, P., and De Schutter, E. (2016).
1374 Multiplexed coding by cerebellar Purkinje neurons. Elife 5.
1375 Houghton, C., and Kreuz, T. (2012). On the efficient calculation of van Rossum
1376 distances. Network 23, 48-58.
1377 Howarth, C., Gleeson, P., and Attwell, D. (2012). Updated energy budgets for neural
1378 computation in the neocortex and cerebellum. J Cereb Blood Flow Metab 32,
1379 1222-1232.
1380 Isler, K., and van Schaik, C.P. (2006). Metabolic costs of brain size evolution. Biol Lett
1381 2, 557-560.
1382 Isope, P., and Barbour, B. (2002). Properties of unitary granule cell-->Purkinje cell
1383 synapses in adult rat cerebellar slices. J Neurosci 22, 9668-9678.
1384 Jack, J.J.B., Noble, D., and Tsien, R.W. (1983). Electric current flow in excitable cells.
1385 (Oxford: Clarendon Press).
1386 Jayant, N., Johnston, J., and Safranek, R. (1993). Signal compression based on models
1387 of human perception. Proceedings of the IEEE 81, 1385 - 1422.
1388 Jörntell, H., and Ekerot, C.F. (2006). Properties of somatosensory synaptic
1389 integration in cerebellar granule cells *in vivo*. J Neurosci 26, 11786-11797.
1390 Kan, P.L.v., Gibson, A.R., and Houk, J.C. (1993). Movement-related inputs to
1391 intermediate cerebellum of the monkey. J Neurophysiol 69, 74-94.
1392 Keele, S.W., and Ivry, R. (1990). Does the cerebellum provide a common
1393 computation for diverse tasks? A timing hypothesis. Ann N Y Acad Sci 608, 179-
1394 207.
1395 Krieger, C., Shinoda, Y., and Smith, A.M. (1985). Labelling of cerebellar mossy fiber
1396 afferents with intra-axonal horseradish peroxidase. Exp Brain Res 59, 414-417.
1397 Lackey, E.P., Heck, D.H., and Sillitoe, R.V. (2018). Recent advances in understanding
1398 the mechanisms of cerebellar granule cell development and function and their
1399 contribution to behavior. F1000Res 7.
1400 Llinás, R., and Sugimori, M. (1980). Electrophysiological properties of in vitro
1401 Purkinje cell dendrites in mammalian cerebellar slices. J Physiol 305, 197-213.
1402 Longair, M.H., Baker, D.A., and Armstrong, J.D. (2011). Simple Neurite Tracer: open
1403 source software for reconstruction, visualization and analysis of neuronal
1404 processes. Bioinformatics 27, 2453-2454.
1405 Marr, D. (1969). A theory of cerebellar cortex. J Physiol (Lond) 202, 437-470.
1406 Martin, T.A., Keating, J.G., Goodkin, H.P., Bastian, A.J., and Thach, W.T. (1996).
1407 Throwing while looking through prisms. I. Focal olivocerebellar lesions impair
1408 adaptation. Brain 119 1183-1198.

1409 Masoli, S., Solinas, S., and D'Angelo, E. (2015). Action potential processing in a
1410 detailed Purkinje cell model reveals a critical role for axonal
1411 compartmentalization. Front Cell Neurosci 9, 47.
1412 Mauk, M.D., and Buonomano, D.V. (2004). The neural basis of temporal processing.
1413 Annu Rev Neurosci 27, 307-340.
1414 Medina, J.F., Garcia, K.S., Nores, W.L., Taylor, N.M., and Mauk, M.D. (2000). Timing
1415 mechanisms in the cerebellum: testing predictions of a large-scale computer
1416 simulation. J Neurosci 20, 5516-5525.
1417 Medina, J.F., and Lisberger, S.G. (2007). Variation, signal, and noise in cerebellar
1418 sensory-motor processing for smooth-pursuit eye movements. J Neurosci 27,
1419 6832-6842.
1420 Mittmann, W., Koch, U., and Häusser, M. (2005). Feed-forward inhibition shapes the
1421 spike output of cerebellar Purkinje cells. J Physiol (Lond) 563, 369-378.
1422 Palay, S.M., and Chan-Palay, V. (1974). Cerebellar cortex: cytology and organization
1423 (Springer, Berlin).
1424 Palkovits, M., Magyar, P., and Szentagothai, J. (1971). Quantitative histological
1425 analysis of the cerebellar cortex in the cat. 3. Structural organization of the
1426 molecular layer. Brain Res 34, 1-18.
1427 Payne, H.L., French, R.L., Guo, C.C., Nguyen-Vu, T.B., Manninen, T., and Raymond, J.L.
1428 (2019). Cerebellar Purkinje cells control eye movements with a rapid rate code
1429 that is invariant to spike irregularity. Elife 8.
1430 Pichitpornchai, C., Rawson, J.A., and Rees, S. (1994). Morphology of parallel fibres in
1431 the cerebellar cortex of the rat: an experimental light and electron microscopic
1432 study with biocytin. J Comp Neurol 342, 206-220.
1433 Pike, F.G., Goddard, R.S., Suckling, J.M., Ganter, P., Kasthuri, N., and Paulsen, O.
1434 (2000). Distinct frequency preferences of different types of rat hippocampal
1435 neurones in response to oscillatory input currents. J Physiol 529 Pt 1, 205-213.
1436 Rakic, P. (1972). Extrinsic cytological determinants of basket and stellate cell
1437 dendritic pattern in the cerebellar molecular layer. J Comp Neurol 146, 335-354.
1438 Raman, I.M., and Bean, B.P. (1997). Resurgent sodium current and action potential
1439 formation in dissociated cerebellar Purkinje neurons. J Neurosci 17, 4517-4526.
1440 Ramón y Cajal, S. (1911). Histologie du Système Nerveux de l'Homme et des
1441 Vertébrés. (A. Maloine, Paris).
1442 Rancz, E.A., Ishikawa, T., Duguid, I., Chadderton, P., Mahon, S., and Häusser, M.
1443 (2007). High-fidelity transmission of sensory information by single cerebellar
1444 mossy fibre boutons. Nature 450, 1245-1248.
1445 Raymond, J.L., and Medina, J.F. (2018). Computational Principles of Supervised
1446 Learning in the Cerebellum. Annu Rev Neurosci 41, 233-253.
1447 Ritzau-Jost, A., Delvendahl, I., Rings, A., Byczkowicz, N., Harada, H., Shigemoto, R.,
1448 Hirrlinger, J., Eilers, J., and Hallermann, S. (2014). Ultrafast action potentials
1449 mediate kilohertz signaling at a central synapse. Neuron 84, 152-163.
1450 Rizwan, A.P., Zhan, X., Zamponi, G.W., and Turner, R.W. (2016). Long-Term
1451 Potentiation at the Mossy Fiber-Granule Cell Relay Invokes Postsynaptic Second-
1452 Messenger Regulation of Kv4 Channels. J Neurosci 36, 11196-11207.

1453 Rossert, C., Dean, P., and Porrill, J. (2015). At the Edge of Chaos: How Cerebellar
1454 Granular Layer Network Dynamics Can Provide the Basis for Temporal Filters.
1455 PLoS Comput Biol 11, e1004515.
1456 Rossum, M.C.W.v. (2001). A Novel Spike Distance. Neural Comput 13, 751-763.
1457 Roth, A., and Häusser, M. (2001). Compartmental models of rat cerebellar Purkinje
1458 cells based on simultaneous somatic and dendritic patch-clamp recordings. J
1459 Physiol 535, 445-472.
1460 Sarnaik, R., and Raman, I.M. (2018). Control of voluntary and optogenetically
1461 perturbed locomotion by spike rate and timing of neurons of the mouse
1462 cerebellar nuclei. Elife 7.
1463 Saviane, C., and Silver, R.A. (2006). Fast vesicle reloading and a large pool sustain
1464 high bandwidth transmission at a central synapse. Nature 439, 983-987.
1465 Serôdio, P., and Rudy, B. (1998). Differential Expression of Kv4 K+Channel Subunits
1466 Mediating Subthreshold Transient K+ (A-Type) Currents in Rat Brain. J
1467 Neurophysiol 79, 1081-1091.
1468 Silver, R.A., Traynelis, S.F., and Cull-Candy, S.G. (1992). Rapid-time-course miniature
1469 and evoked excitatory currents at cerebellar synapses in situ. Nature 355, 163-
1470 166.
1471 Singla, S., Dempsey, C., Warren, R., Enikolopov, A.G., and Sawtell, N.B. (2017). A
1472 cerebellum-like circuit in the auditory system cancels responses to self-generated
1473 sounds. Nat Neurosci 20, 943-950.
1474 Soltesz, I., and Losonczy, A. (2018). CA1 pyramidal cell diversity enabling parallel
1475 information processing in the hippocampus. Nat Neurosci 21, 484-493.
1476 Spanne, A., and Jörntell, H. (2013). Processing of multi-dimensional sensorimotor
1477 information in the spinal and cerebellar neuronal circuitry: a new hypothesis.
1478 PLoS Comput Biol 9, e1002979.
1479 Steuber, V., Mittmann, W., Hoebeek, F.E., Silver, R.A., De Zeeuw, C.I., Häusser, M., and
1480 De Schutter, E. (2007). Cerebellar LTD and pattern recognition by Purkinje cells.
1481 Neuron 54, 121-136.
1482 Sudhakar, S.K., Hong, S., Raikov, I., Publio, R., Lang, C., Close, T., Guo, D., Negrello, M.,
1483 and De Schutter, E. (2017). Spatiotemporal network coding of physiological
1484 mossy fiber inputs by the cerebellar granular layer. PLoS Comput Biol 13,
1485 e1005754.
1486 Sultan, F., and Bower, J.M. (1998). Quantitative Golgi study of the rat cerebellar
1487 molecular layer interneurons using principal component analysis. J Comp Neurol
1488 393, 353-373.
1489 Suvrathan, A., Payne, H.L., and Raymond, J.L. (2016). Timing rules for synaptic
1490 plasticity matched to behavioral function. Neuron 92, 959-967.
1491 Tsodyks, M.V., and Markram, H. (1997). The neural code between neocortical
1492 pyramidal neurons depends on neurotransmitter release probability. Proc Natl
1493 Acad Sci U S A 94, 719-723.
1494 Valera, A.M., Binda, F., Pawlowski, S.A., Dupont, J.L., Casella, J.F., Rothstein, J.D.,
1495 Poulain, B., and Isope, P. (2016). Stereotyped spatial patterns of functional
1496 synaptic connectivity in the cerebellar cortex. Elife 5.

1497 Valera, A.M., Doussau, F., Poulain, B., Barbour, B., and Isope, P. (2012). Adaptation of
1498 granule cell to purkinje cell synapses to high-frequency transmission. J Neurosci
1499 32, 3267-3280.
1500 van Kan, P.L., Gibson, A.R., and Houk, J.C. (1993). Movement-related inputs to
1501 intermediate cerebellum of the monkey. J Neurophysiol 69, 74-94.
1502 van Rossum, M.C. (2001). A novel spike distance. Neural Comput 13, 751-763.
1503 Vranesic, I., Iijima, T., Ichikawa, M., Matsumoto, G., and Knöpfel, T. (1994). Signal
1504 transmission in the parallel fiber-Purkinje cell system visualized by high-
1505 resolution imaging. Proc Natl Acad Sci U S A 91, 13014-13017.
1506 Wadiche, J.I., and Jahr, C.E. (2005). Patterned expression of Purkinje cell glutamate
1507 transporters controls synaptic plasticity. Nat Neurosci 8, 1329-1334.
1508 Wagner, M.J., Kim, T.H., Savall, J., Schnitzer, M.J., and Luo, L. (2017). Cerebellar
1509 granule cells encode the expectation of reward. Nature 544, 96-100.
1510 Wallace, G.K. (1992). The JPEG still picture compression standard. IEEE
1511 Transactions on Consumer Electronics 38, xviii - xxxiv.
1512 Walter, J.T., and Khodakhah, K. (2009). The advantages of linear information
1513 processing for cerebellar computation. Proc Natl Acad Sci U S A 106, 4471-4476.
1514 Wang, W.C., and Brehm, P. (2017). A Gradient in Synaptic Strength and Plasticity
1515 among Motoneurons Provides a Peripheral Mechanism for Locomotor Control.
1516 Curr Biol 27, 415-422.
1517 Williams, R.W., and Herrup, K. (1988). The control of neuron number. Annu Rev
1518 Neurosci 11, 423-453.
1519 Wilms, C.D., and Häusser, M. (2015). Reading out a spatiotemporal population code
1520 by imaging neighbouring parallel fibre axons in vivo. Nat Commun 6, 6464.
1521 Witter, L., Canto, C.B., Hoogland, T.M., de Gruijl, J.R., and De Zeeuw, C.I. (2013).
1522 Strength and timing of motor responses mediated by rebound firing in the
1523 cerebellar nuclei after Purkinje cell activation. Front Neural Circuits 7, 133.
1524 Witter, L., and De Zeeuw, C.I. (2015a). In Vivo Differences in Inputs and Spiking
1525 Between Neurons in Lobules VI/VII of Neocerebellum and Lobule X of
1526 Archaeocerebellum. Cerebellum 14.
1527 Witter, L., and De Zeeuw, C.I. (2015b). Regional functionality of the cerebellum. Curr
1528 Opin Neurobiol 33, 150-155.
1529 Xiao, J., Cerminara, N.L., Kotsurovskyy, Y., Aoki, H., Burroughs, A., Wise, A.K., Luo, Y.,
1530 Marshall, S.P., Sugihara, I., Apps, R., and Lang, E.J. (2014). Systematic regional
1531 variations in Purkinje cell spiking patterns. PLoS ONE 9, e105633.
1532 Yamazaki, T., and Tanaka, S. (2007). A spiking network model for passage-of-time
1533 representation in the cerebellum. Eur J Neurosci 26, 2279-2292.
1534 Zhou, H.B., Lin, Z.M., Voges, K., Ju, C.H., Gao, Z.Y., Bosman, L.W.J., Ruigrok, T.J.,
1535 Hoebeek, F.E., De Zeeuw, C.I., and Schonewille, M. (2014). Cerebellar modules
1536 operate at different frequencies. Elife 3.

1537

1538